

A Faulting Model for the 1979 Imperial Valley Earthquake

RALPH J. ARCHULETA

U.S. Geological Survey

By comparing synthetic particle velocities with the near-source strong motion data we have constructed, by trial and error, a faulting model for the 1979 Imperial Valley earthquake. The calculation of the synthetic seismograms takes into account the vertical inhomogeneity of the elastic parameters in the Imperial Valley and the spatial variation of the slip rate parameters on the fault plane. The independent slip rate parameters are (1) the strike-slip rate amplitude, (2) the dip-slip rate amplitude, (3) the duration that slip rate is nonzero (the rise time of the slip function) and (4) the rupture time, which determines when the slip rate is initiated. Our faulting model has the following principal features: (1) Faulting occurred on the Imperial fault and on the Brawley fault, rupture on the Brawley fault being triggered by rupture on the Imperial fault. (2) The Imperial fault is a plane 35 km long and 13 km wide with a strike of 323°, measured clockwise from north, and a dip of 80° NE. The Brawley fault is a 10 km long and 8 km wide plane with a strike of 360° and a dip of 90°. (3) Faulting on the Imperial fault is primarily right-lateral strike slip with a small component of normal dip slip in the sediments at its northern end. The larger strike-slip rates are generally confined between depths of 5 and 13 km with maximum values of about 1.0 m/s. The duration varies on the fault with a maximum of 1.9 s, which is considerably shorter than the total time for the rupture to take place. (4) The rupture velocity on the Imperial fault is highly variable. Locally, it exceeds the shear wave velocity and, in one instance, the compressional wave velocity. The average rupture velocity, though, is less than the shear wave velocity. (5) Although the slip on the Brawley fault contributes only about 4% of the total moment, it greatly affects the ground motion at nearby stations. (6) The total seismic moment is 6.7×10^{18} N m where the Imperial fault contributes 6.4×10^{18} N m and the Brawley fault contributes 2.7×10^{17} N m. In the process of trying almost 300 faulting models, we found that given the elastic parameters of the medium, the synthetic seismograms were most sensitive to the specification of the rupture time. Although the slip rate amplitudes are linearly related to the data, the rupture time and the duration are not. The parameterization of the nonlinear variables has a strong effect on the generation of synthetic seismograms from a finite fault.

INTRODUCTION

In terms of near-source observations of ground accelerations and surface offsets the Imperial Valley earthquake of October 15, 1979, is the best documented earthquake ever recorded [Johnson *et al.*, 1982]. The abundance and quality of these near-source observations presents an unparalleled opportunity for studying the mechanism of a moderate sized earthquake M_L 6.6 [Chavez *et al.*, 1982], $M_0 = 7.0 \times 10^{18}$ N m [Kanamori and Regan, 1982]. The results presented in this paper are determined from analysis of an important subset of all the data: time histories of the ground velocities determined from accelerograms recorded in the United States [Brady *et al.*, 1982].

Hartzell and HelMBERGER [1982], [Olson and Apsel [1982] and Hartzell and Heaton [1983] have presented faulting models and synthetics for the Imperial Valley earthquake based on analyses of almost the same data. The basic features of their faulting models are described below. Hartzell and HelMBERGER [1982] used a forward modeling approach to compute near-source displacements in the frequency range 0.0–1.0 Hz for comparison with the doubly integrated accelerograms recorded in the United States. The basic features of the Hartzell and HelMBERGER faulting model are the following:

1. Slip occurs on a vertical Imperial fault assumed to be 10.5 km deep and 36 km long. It extends unilaterally from the epicenter along a strike of 323°, measured clockwise from

north, with a notable S-shaped deviation in the strike in the range 14–24 km measured from their epicenter.

2. The slip rate function is a triangle with a constant 1.0-s duration and constant rake of 180°.

3. The rupture velocity is a constant 2.5 km/s.

4. The slip rate distribution shows the largest amplitudes, greater than 1.0 m/s, in the depth range of 4–9 km with two distinct areas, distances of 8 and 18 km northwest of the epicenter, having average amplitudes of 2.5 m/s.

5. The static slip has the same distribution as the slip rate with a maximum value of 2.5 m; the seismic moment is 5.0×10^{18} N m.

Olson and Apsel [1982] used a constrained least squares inversion of low-passed accelerograms, 0.0–0.33 Hz, recorded in the United States and Mexico to determine a faulting model of the Imperial Valley earthquake. They divided the fault planes into $5 \text{ km} \times 5 \text{ km}$ squares and allowed slip to occur in five 0.75-s windows. The basic features of the Olson and Apsel model are as follows:

1. They assume that slip occurs on a vertical Imperial fault 10 km deep and 50 km long with 40 km northwest of the epicenter and 10 km southeast; the Imperial fault has a constant strike of 323°; they include a vertical Brawley fault 10 km deep and 10 km long; the Brawley fault has a constant strike of 360°; both faults have dips of 90°.

2. The slip rate has both strike-slip and dip-slip components. Its time function is basically a rectangle with a duration about 1.5 s.

3. Although a rupture velocity is specified (0.9 times the local shear wave velocity V_s), the slip, in a given fault element, may commence as much as 1.5 s before or after the time determined by this specified velocity; for depths be-

This paper is not subject to U.S. copyright. Published in 1984 by the American Geophysical Union.

Paper number 3B1760.

tween 5 and 10 km they inferred a supershear rupture velocity between 4.0 and 5.0 km/s for a 20-km-long section of the Imperial fault.

4. The slip rate amplitude is primarily strike slip with a small component of dip slip at the northern end of the Imperial fault and on the Brawley fault. The amplitudes smoothly vary along the strike of the Imperial fault with a maximum value of about 1.2 m/s at depths of 5–10 km in the epicentral range of 20–25 km.

5. The final offset has a maximum value of 1.6 m in the epicentral range of 15–20 km; the seismic moment is 9.1×10^{18} N m.

Hartzell and Heaton [1983] used an inversion method similar to that of Olson and Apsel. However, the data they inverted were the horizontal components of the particle velocity time histories in the 0.1- to 1.0-Hz passband and some long-period teleseismic *P* wave records. Hartzell and Heaton subdivided the Imperial fault into elements 3 km long and 2.5 km wide. After trying about 30 different inversions they prefer a model that has the following properties:

1. Slip occurs on the Imperial fault assumed to be 10 km deep and 42 km long with 36 km northwest of their epicenter. The strike is 323° ; the dip is 90° .

2. The slip rate function has both strike-slip and dip-slip components. The time function is 1.7 s in duration but divided into three segments (0.7, 0.5, and 0.5 s). Thus for each element of the fault, slip can occur at three times, each of which can have a different amplitude.

3. The rupture velocity of $0.85V_s$, where V_s is the local shear wave velocity, is specified, but slip in each element of the fault plane may begin at or after (up to 1.75 s) the time determined by the rupture velocity.

4. There is a small component of dip slip generally confined to shallow depths. The strike-slip rates dominate with a maximum of the order of 1.5 m/s that occurs about 16–20 km north of their epicenter and at depths between 6 and 8 km.

5. The final slip has a maximum value of about 1.8 m in the same area of maximum slip rates; the seismic moment is 4.9×10^{18} N m.

Although these faulting models exhibit similarities in their spatial distribution and amplitudes of the slip rate and in the approximate duration of slip, the fit of the synthetics to the data is much different among the three models. Olson and Apsel's synthetics generally match the phase of the first arriving energy extremely well, but the amplitudes are almost always too small by about a factor of two or more on one or both of the horizontal components for stations within 10 km of the fault, with the exception of Meloland. The synthetic displacements computed by Hartzell and Helmburger do not agree nearly as well in phase with the data as those of Olson and Apsel. Although it is difficult to compare corresponding amplitudes in the Hartzell and Helmburger synthetics, the 230° component is at least a factor of two larger than the data near the fault with the difference decreasing as one moves farther from the fault. On the other hand, the 140° synthetic is generally smaller than the data near the fault but becomes larger than the data as one moves farther from the fault. Hartzell and Heaton's synthetics match the phases of the first arriving energy very well. Although pulse shapes after the first one are not as well matched, they are similar to the data. For stations near the fault the peak amplitude of the particle velocity on the 230°

horizontal is about half the amplitude of the synthetic; for stations more than 5 km off the fault the data always exceed the synthetic amplitudes and are about twice as large for stations more than 10 km from the fault. The 140° (320°) synthetic is almost always less than the data, with the difference becoming larger as the stations move farther from the fault.

There are two disturbing aspects of these faulting models. First, the synthetics generated misfit the largest near-source amplitudes by about a factor of two or more; second, the synthetic amplitudes show a much different dependence on distance from the fault than the data. Whether the maximum near-source particle velocities are 1.0, 2.0, or 0.5 m/s is very important to earthquake engineers. Whether the peak amplitudes decay rapidly or slowly with increasing distance from the fault or perhaps remain constant out to a certain distance is an important consideration in evaluating earthquake hazards in the near-source region. It is clear that if one were to use a regression analysis [e.g., Joyner and Boore, 1981] for the data and for the synthetics in the same passband, the resulting coefficients would be substantially different. In addition to the engineering considerations, there is the disparity between the Olson and Apsel [1982] model and the Hartzell and Heaton [1983] model of the faulting mechanism. Since neither model produces a substantially better fit between synthetics and the data, each is an equally valid, yet different, explanation for the earthquake.

In this paper we present a faulting model that generates synthetic seismograms that agree within 50% or less with almost all of the near-source particle velocity records in the United States. First, we discuss the general features of the data that we consider important and should be explained by the faulting model. Next, we discuss our approach to this problem in terms of the parameters constituting a faulting model. We try to point out what parameters are fixed by initial assumptions and what parameters are being solved for. Following the discussion of the method we describe our preferred faulting model. Next, we discuss the fit between the synthetics and data. We emphasize how key elements of the faulting model were constrained by the data. Finally, we try to summarize how the characteristics of our faulting model for the Imperial Valley earthquake fit into a more general description of earthquake mechanics and how they imply a greater degree of seismic risk.

DATA

Before discussing the method and subsequent analysis, we first want to describe the data set. The true data are the accelerograms recorded in the United States [Brady *et al.*, 1982; Porter, 1982]. However, the data which we will use are the particle velocity time histories obtained by integrating and low passing the processed accelerograms. Figure 1 shows a map view of the Imperial Valley with the accelerograph locations relative to the epicenter [Archuleta, 1982a] and to the Imperial and Brawley faults on which surface slip was measurable [Sharp *et al.*, 1982]. The three-letter station names are the officially assigned codes for strong motion instruments in the United States [Switzer *et al.*, 1981]. Nine additional accelerographs in Baja California, Mexico, recorded the main shock [Brune *et al.*, 1982]. In this paper we do not consider the Mexican stations, though they would probably increase the resolution of the faulting model in the hypocentral area. It is unlikely that a significant amount of

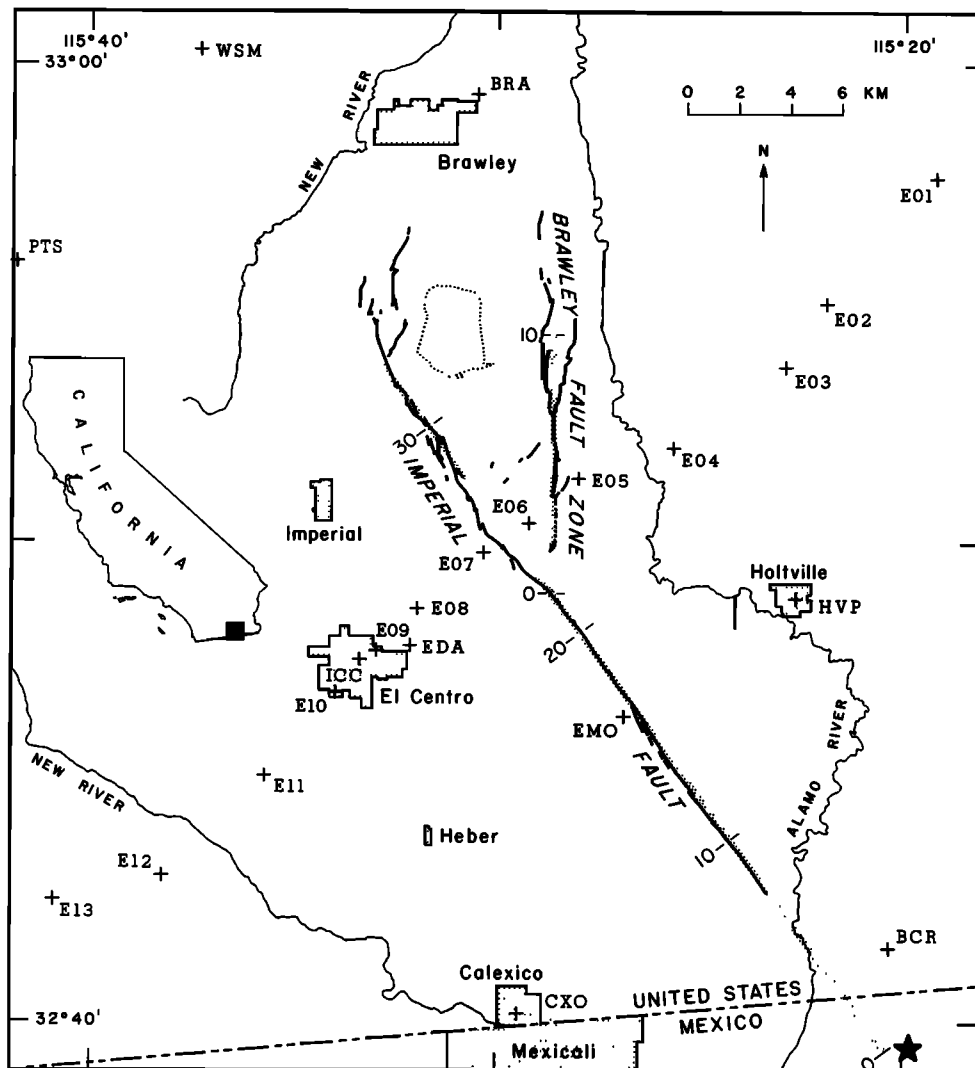


Fig. 1. Map view of the Imperial Valley area showing locations of accelerographs in the United States (pluses), parts of the Imperial fault and Brawley fault zone where surface offsets were measured, the location of the epicenter [Archuleta, 1982a] (indicated by a star), and geographical features such as the international border and local communities. The general strike of the Imperial fault is 323° , measured clockwise from north; the strike of the Brawley fault zone is about 360° . The linear stipled regions show the fault traces as we have modeled them. Distances are shown along the traces. The shaded box on the inserted outline of the state of California shows the approximate region for the Imperial Valley area.

slip occurred south of the epicenter; any such slip that might have occurred does not strongly affect the motion recorded at the stations in the United States with the exception of Calexico (CXO) and Bonds Corner (BCR).

In Figures 2-4 the low passed particle velocity time histories are plotted on the same map view as Figure 1. The data shown in Figures 2-4 have been low passed with a zero-phase shift, two-pole Butterworth filter with a corner frequency of 0.5 Hz. Similar plots of unfiltered particle velocity and acceleration time histories along with a discussion of the data are given by Archuleta [1982b]. We do not analyze frequencies greater than 1.0 Hz in this paper. The horizontal (323° , measured clockwise from north) particle velocity is motion parallel to the general strike of the Imperial fault; the (53°) horizontal particle velocity is motion perpendicular to the general strike on the Imperial fault. Positive amplitudes correspond to particle velocities directed down, along a 323° azimuth, and along a 53° azimuth in Figures 2, 3, and 4,

respectively. The filtered data give, in some respects, a more reliable picture for comparing the ground motion among the stations since the lower frequencies are less affected by small-scale irregularities in the velocity structure. Although the dynamic and static data have been discussed by Archuleta [1982b], Hartzell and Helmberger [1982], Niazy [1982], and others, there are some important points worth reiterating.

The horizontal S wave amplitudes are asymmetric, with the stations east of the Imperial fault having the larger amplitudes. This is clearly seen in both the 53° component (Figure 4) and the 323° component (Figure 3). The easiest way to produce the asymmetry is by a NE dip on the Imperial fault, since a single vertical fault in a laterally homogeneous medium cannot produce this asymmetry. However, another possibility is slip on the Brawley fault which Cohn *et al.* [1982] show had surface slip at nearly the same time as slip occurred on the Imperial fault. Either a NE

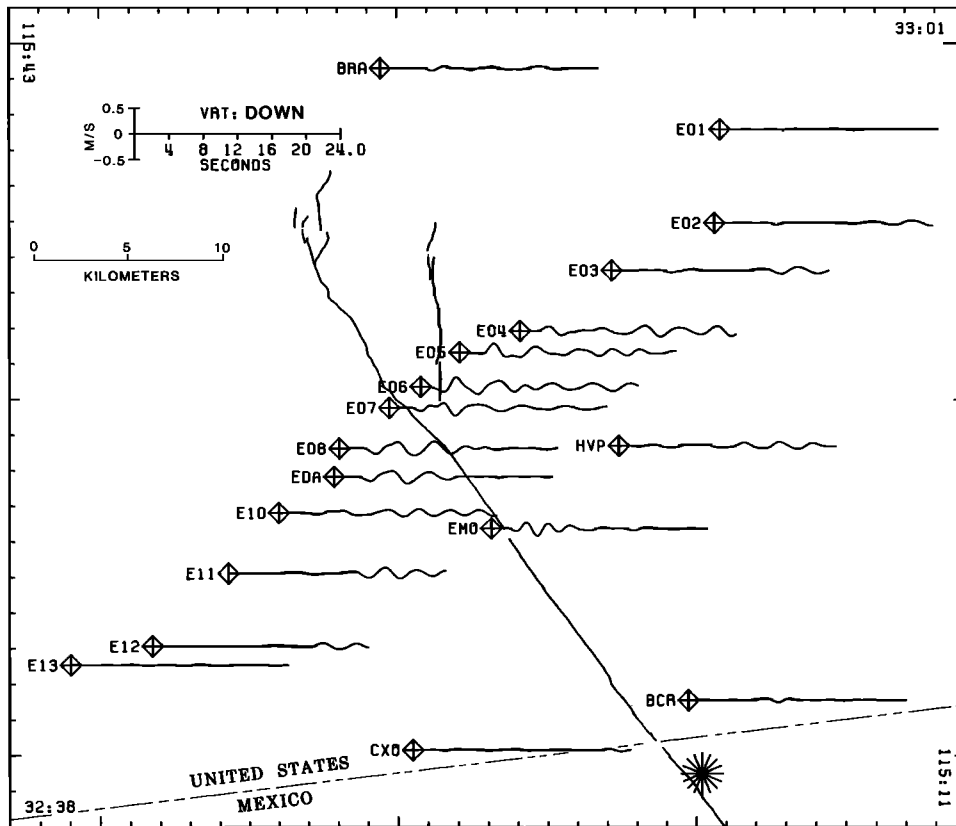


Fig. 2. Low passed vertical components of particle velocity time histories are superposed on a map view of the Imperial Valley region. The first 24 s at each station after the accelerographs triggered are plotted. Traces have been low passed filtered using a two-pole zero-phase shift Butterworth filter with a corner frequency of 0.5 Hz. Positive motion on the traces is down, into the earth. The amplitude scale and time scale are shown near the upper left corner. The surface traces of the Imperial fault and Brawley fault zone are shown. The epicenter is shown by the star.

dip on the Imperial fault or slip on the Brawley fault or a combination of the two will destroy symmetry in the particle motion. Particular notice should be taken of stations E03 and E11. These two stations are within 0.5 km of perfect symmetry around the trace of the Imperial fault. The amplitude of the horizontal components at E03 is almost twice that of E11, however. This asymmetry in amplitudes persists even for stations E06 and E07 which are 2 km apart but on opposite sides of the trace of the Imperial fault.

The amplitude of the 323° component at stations E06 and E07 (Figure 3) is clearly not nodal, as one would expect from a rupture on a vertical fault, nor are the 323° waveforms at E06 and E07 reflections of each other, as would be predicted from rupture on a single vertical fault that passed between the two stations.

The strong pulse that immediately follows the direct S wave is a prominent feature of the 53° component particle velocities. Considering the geometry of the Imperial fault, the location of the stations, and the epicenter, a rupture propagating northwest along the Imperial fault will produce strong S wave motion in the 233° direction. This is clearly observed at stations close to the fault (e.g., E05, E06, E07, and EM0) (Figure 4). The large pulse in the 53° direction that immediately follows the first motion in the 233° direction is not so easily explained, however. At station E05 this pulse in the 53° direction is larger than the pulse due to the direct S waves from the southern part of the Imperial fault.

The vertical component of motion for stations near the

fault (Figure 2) is distinctly antinodal. A rather lengthy discussion of the large-amplitude vertical acceleration records and possible causes for the vertical motion is given by Archuleta [1982b]. His primary hypothesis was that the vertical motion was caused by the caustic of a PP type phase that exists because of a strong gradient in the P wave velocity structure in the upper 5 km of the Imperial Valley [McMechan and Mooney, 1980]. His secondary hypothesis was that the large vertical accelerations could be caused by sudden changes in the rupture velocity which would have to exceed the S wave velocity in order that directivity affect the P wave radiation pattern.

METHOD

The fundamental theorem for kinematic modeling and the basis of our approach is the representation theorem [Maruyama, 1963; Burridge and Knopoff, 1964]

$$\dot{u}_i(\mathbf{y}, t) = \int_0^t dt' \iint_A \dot{\mathbf{s}}(\mathbf{x}, t', T, \tau) \cdot \mathbf{T}^i(\mathbf{x}, t-t'; \mathbf{y}) dA \quad (1)$$

where $\dot{u}_i(\mathbf{y}, t)$ is the i th ($i = 1, 2, 3$) component of particle velocity at spatial coordinate \mathbf{y} and time t ; $\dot{\mathbf{s}}(\mathbf{x}, t', T, \tau)$ is the slip rate vector at fault coordinate \mathbf{x} and time t' ; $\mathbf{T}^i(\mathbf{x}, t-t'; \mathbf{y})$ is the traction per unit impulse at the fault coordinate \mathbf{x} , due to a point force applied in the i th direction at the observer location \mathbf{y} ; dA is an incremental area of the fault plane with total area A ; the double integrals are for summation of the

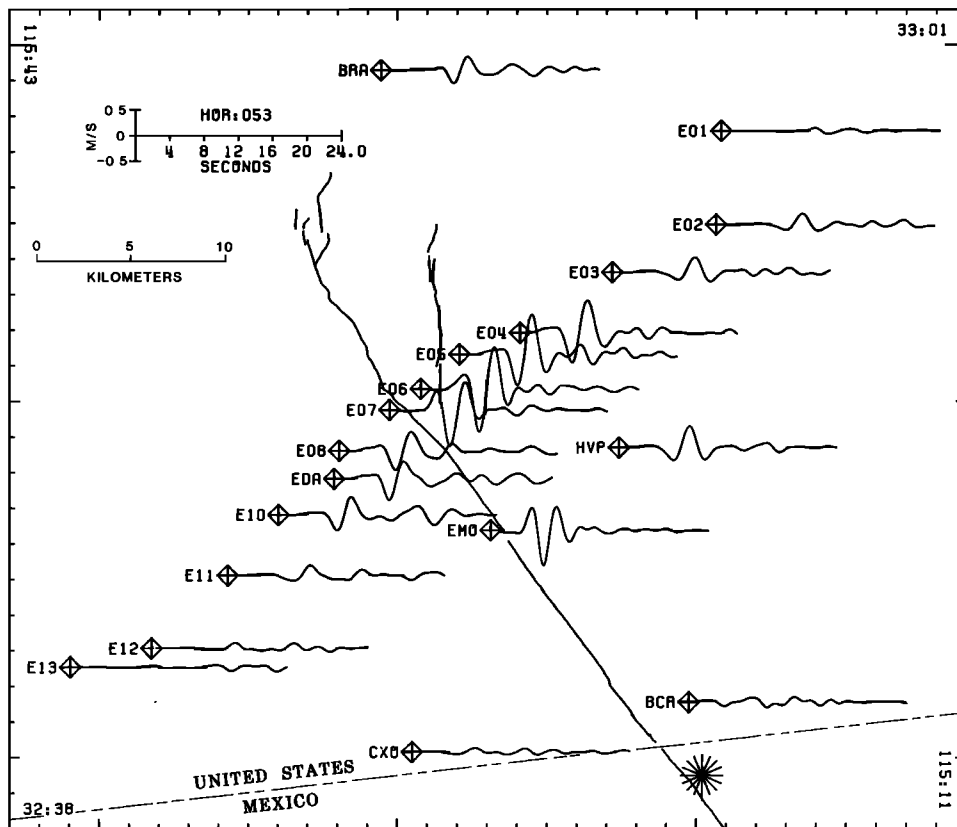


Fig. 3. Low passed 323° horizontal component of particle velocity superposed on a map view of the Imperial Valley. Positive amplitudes correspond to motion directed along the 53° azimuth, measured clockwise from north; negative amplitudes correspond to motion directed along the 143° azimuth. This horizontal motion is parallel to the general strike of the Imperial fault. See caption of Figure 2 for geographical details.

kernel over the entire fault plane; and the single integral on dt' is for the temporal convolution of $\dot{s} \cdot T^i$. A derivation of (1) is given by Spudich [1980]. Figure 5 shows a schematic display of the observer and fault geometry as well as a general slip rate function that we will use throughout our discussion. The observer coordinates are defined by orthogonal vectors y_1 , y_2 , and y_3 ; the fault coordinates are defined by orthogonal vectors x_1 , x_2 . Both coordinate systems share the same origin. In the case of the Imperial Valley earthquake we take the point on the Imperial fault's surface trace closest to the epicenter for the origin (Figure 1).

In dissecting this equation we can understand what constitutes a faulting model, since there are parts of this equation that contribute to \dot{u}_i independent of the fracture process, while other parts are completely determined by the fracture process. The parts of the representation theorem that depend on the fracture process constitute a description of the earthquake mechanism. Furthermore, we can see the different stages at which assumptions are made. The point at which an assumption is made is critical in that all subsequent analysis depends on it.

Traction Vector (Green's Functions)

First, we consider the part of the representation theorem that is independent of the fracture process, namely, the traction $T^i(x, t-t'; y)$. As noted above, these tractions result from application of a point force on the fault surface and are thus a form of the Green's functions of the medium. The

traction depends on the elastic properties of the medium and on the location of the fault plane. Because the traction is independent of the fracture process, it can be determined from data unrelated to the data being studied. Fortunately for the Imperial Valley, the velocity structure is well known. A detailed refraction survey [Fuis *et al.*, 1982] of the Imperial Valley region was conducted 7 months before the main shock. From analysis of this data, Fuis *et al.* [1982] and McMechan and Mooney [1980] determined the P wave velocity structure. By combining the P wave velocity structure with gravity profiles in the region Fuis *et al.* also estimated the density structure. Archuleta *et al.* [1979] estimated the S wave velocity structure deeper than 300 m by using S wave recordings of aftershocks of the Imperial Valley main shock [Boore and Fletcher, 1982] and similarity with the P wave velocity/depth profile. For depths less than 300 m, the S wave velocity profile is based on drill logs in the Imperial Valley [Shannon and Wilson, Inc., and Agabian Associates, 1976]. As expected, the velocity structure is not laterally homogeneous [Fuis *et al.*, 1982]. However, combining the accelerographs locations, the Imperial fault, and the different velocity profiles of Fuis *et al.* [1982], the assumption of a laterally homogeneous medium is a reasonable approximation for timing accuracy of the order of 0.5 s. The assumption of lateral homogeneity with a 0.5-s timing error is further supported by the P wave travel time delay map that is a composite map for all the shot points in the Imperial Valley [Kohler and Fuis, 1983]. The travel time delay map shows that in the regions of the Imperial Valley, where the

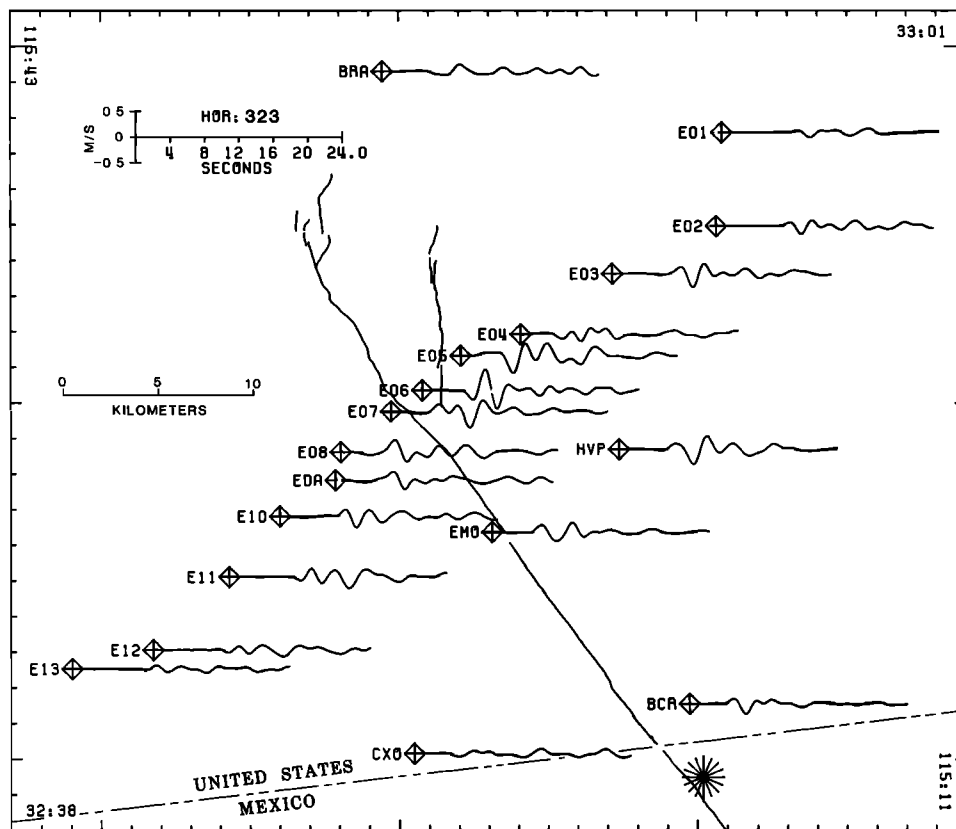


Fig. 4. Low passed 53° horizontal component of particle velocity superposed on a map view of the Imperial Valley. Positive amplitudes correspond to motion directed along the 323° azimuth, measured clockwise from north; negative amplitudes correspond to motion directed along the 233° azimuth. This horizontal motion is perpendicular to the general strike of the Imperial fault. See caption of Figure 2 for geographical details.

accelerographs are located, the maximum difference in P wave travel times is about 0.25 s. Only stations E12 and E13 are in regions of rapidly changing P wave delays.

Having assumed a laterally homogeneous medium with a given set of vertically varying elastic parameters, we compute the Green's functions up to a maximum frequency of 1.0 Hz. To avoid ringing in the synthetics, the amplitude spectrum of each synthetic is cosine tapered between 0.5 and 1.0 Hz. The Green's functions, computed using the discrete wave number/finite element (DWFE) method [Olson *et al.*, 1983], include all body wave types, surface waves, leaky modes, and near-field terms and account for gradients as well as discontinuities in the velocity structure.

Having data that constrain the velocity structure is invaluable. Before computing T^i , it is necessary to know the location of the fault, which we assume to be a plane with a constant strike and dip. The general strike, 323°, of the Imperial fault is well known. The dip of the Imperial fault is not well determined. For computation ease we prefer to have a constant dip, though the refraction results [Fuis *et al.*, 1982] show that the dip on the Imperial fault may vary by 8° from the southeast end to the northwest end. Archuleta [1982b] used three lines of evidence to deduce an approximate 75° NE dip for the Imperial fault. Though the dip angle can, in theory, be determined independently of the data being studied, we varied the dip angle to find the value that gives the best match between data and synthetics. We used constant dip angles of 75° NE, 80° NE, and 90°. An 80° NE dip angle is used in the best fitting fault model.

Limits of Integration and Slip Rate Parameters

The parameters that constitute the earthquake mechanism separate into two groups: the boundaries of the faulting which prescribe the limits of integration and the description of the slip rate function. The length and width of the faulted area are not always easily determined. Fortunately, the Imperial Valley earthquake had substantial surface slip and a well-determined epicenter [Archuleta, 1982a], thus giving a good approximate length of 35 km northwest of the epicenter. The lack of observed surface slip [Sharp *et al.*, 1982] in the epicentral area leaves unresolved the question of how much slip at depth occurred south of the epicenter. The inversion results of Olson and Apsel [1982] indicate that slip occurred on a 10-km segment southeast of the epicenter. Since this paper does not consider the strong motion at stations in Baja California, Mexico, the data most affected by any slip on the Imperial fault south of the epicenter, we will use a fault plane that begins at the epicenter and extends northwest 35 km along a constant strike of 323°, measured clockwise from north (Figure 1).

Although the length of faulting for the Imperial Valley earthquake is rather tightly constrained, the depth of faulting is not. Archuleta [1982b] suggests that 10 km is a reasonable value. Our best fitting faulting model has a width of 13 km, though we tried more than 150 models with a width of 10 km. Although a reasonable fit between the synthetic seismograms and the data can be found using a width of 10 km, so much of the slip was concentrated near 10-km depth that

there was an abrupt transition from nonzero slip to zero slip [e.g., Hartzell and Heaton, 1983]. By increasing the width to 13 km the fit between the synthetics and data improved as well as the smoothness of the slip distribution.

The final set of parameters necessary to compute the synthetic seismograms is the slip rate function $\dot{s}(\mathbf{x}, t, T, \tau)$. In general, it is the specification of these parameters that constitutes the bulk of the work in forward and inversion modeling, since the geometrical constraints and the velocity structure are often held fixed to initial values. Because we are specifying the slip rate function, the model is by definition a kinematic model. The very first assumption made in specifying a slip rate function is the functional form. For our purposes we have assumed a rectangle $\dot{s} = |\dot{s}| [H(t-T) - H(t-T-\tau)] \hat{s}$ where \hat{s} is a unit vector, $|\dot{s}|$ is the amplitude of \dot{s} , and $H(t)$ is the Heaviside function. On the basis of results from the fully dynamic models and quasi-dynamic models, a more appropriate guess might be a modified Kostrov [1964] slip rate function [Boatwright, 1980; Archuleta and Hartzell, 1981]. However, at the low frequencies being modeled, a low passed modified Kostrov function is quite similar to a rectangle. There are four parameters that must be specified everywhere on the fault plane to describe the slip rate: (1) the slip rate amplitude of the strike-slip component, (2) the slip rate amplitude of the dip-slip component, (3) the rupture time T that the slip rate first becomes nonzero (this rupture time determines the rupture velocity or vice versa), (4) a rise time variable (τ) that is the duration the slip rate is nonzero after being activated. These four variables are all functions of the fault plane coordinates (x_1, x_2). Depending on one's a priori knowledge about the faulting process or computational difficulty, simplifying assumptions are often made about these four parameters [e.g., Aki, 1968; Anderson and Richards, 1975; Heaton and Helmberger, 1979; Bouchon, 1982]. For example, the Hartzell and Helmberger [1982] model assumes that everywhere on the fault the dip-slip component is zero, the rise time is a constant, and the rupture velocity is

TABLE 1. Elastic Parameters for the Imperial Valley

Depth, km	V_p , km/s	V_s , km/s	ρ , kg/m ³
0	1.70	0.40	1800
0.4	1.80	0.70	1800
5.0	5.65	3.20	2500
11.0	5.85	3.30	2800
11.0	6.60	3.70	2800
12.0	7.20	4.15	2800

Between any two successive depths, linear interpolation is used to determine intermediate values. A half space exists for depths greater than 12 km. Different elastic parameters at the same depth indicate a discontinuity.

a constant. While it is important to understand the basis for making any approximation regarding the slip rate function, it is equally important to realize that making an approximation about one of the parameters does not lessen the significance of that parameter in the description of the faulting model.

We want to call attention to a very important feature in the relation between $\dot{s}(\mathbf{x}, t, T, \tau)$ and $u_i(\mathbf{y}, \tau)$; \dot{s} can be written

$$\dot{s}(\mathbf{x}, t, T, \tau) = |\dot{s}(\mathbf{x})| [H(t-T(\mathbf{x})) - H(t-T(\mathbf{x}) - \tau(\mathbf{x}))] \hat{s} \quad (2)$$

If one were to substitute (2) into (1), it is true that the data are linearly related to the slip rate amplitude, but the data are not linearly related to the two temporal parameters T and τ . The linearity between the slip rate amplitude and the data forms the basis for the inversion methods of Spudich [1980], Olson and Apsel [1982], and Hartzell and Heaton [1983]. In the latter two methods, some a priori parameterization of the temporal variables must be made before inverting the data to obtain a distribution of slip rate amplitudes.

Another aspect of the kinematic modeling that (2) highlights is the trade-off between rupture velocity, determined by $T(\mathbf{x})$, and the duration $\tau(\mathbf{x})$ which has been demonstrated by Anderson and Richards [1975]. Although a trade-off exists, the results of Anderson and Richards show that it takes a 300% change in duration to compensate for a 17% change in rupture velocity. Although we cannot quantify the trade-off, it is clear that the parameters $\tau(\mathbf{x})$ and $T(\mathbf{x})$ can trade-off in the second term of (2) but not in the first term, which involves only $T(\mathbf{x})$.

FAULTING MODEL

Forward Modeling

In the more than 300 faulting models we have tried, almost every parameter has been varied. The final Green's functions are computed using the elastic parameters given in Table 1. In our first approximation we used a surficial S wave velocity of 800 m/s, about a factor of four larger than the data [Shannon and Wilson, Inc., and Agabian Associates, 1976]. To improve the timing between P and S waves and to improve the timing between S and SS phases, we decided on a 400 m/s surficial velocity as a compromise between computational costs and a better fit between the synthetics and the data. We assumed a maximum fault length of 35 km from the epicenter for the Imperial fault. We determined that a plane dipping 80° NE with a maximum plunge of 13 km gave the best results. With the elastic properties of the medium and the geometry of the Imperial fault fairly well set, we would assume a slip rate function $\dot{s}(\mathbf{x}, t, T, \tau)$ and compute synthetic seismograms [Spudich,

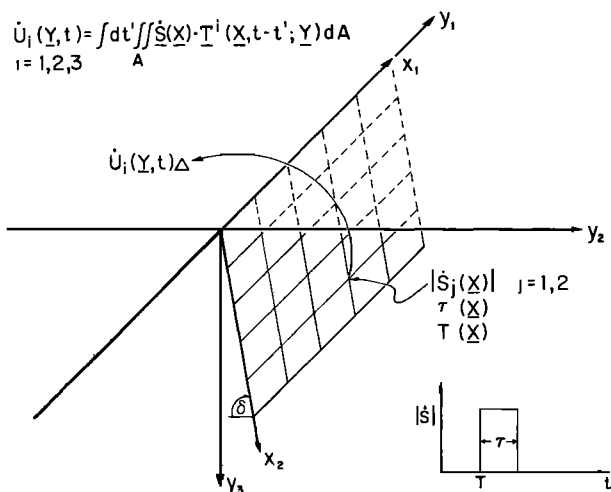


Fig. 5. Schematic picture of the parameters necessary to evaluate the representation theorem. The observer coordinates are designated by Y_i ; the fault plane coordinates by X_j . The dip of the fault is shown by δ . The slip rate function is defined by four parameters: \dot{S}_1 (strike-slip rate), \dot{S}_2 (dip-slip rate), T (rupture time) and (duration) all of which can vary as a function of X_1, X_2 . In our case the medium is allowed to be vertically inhomogeneous but laterally homogeneous.

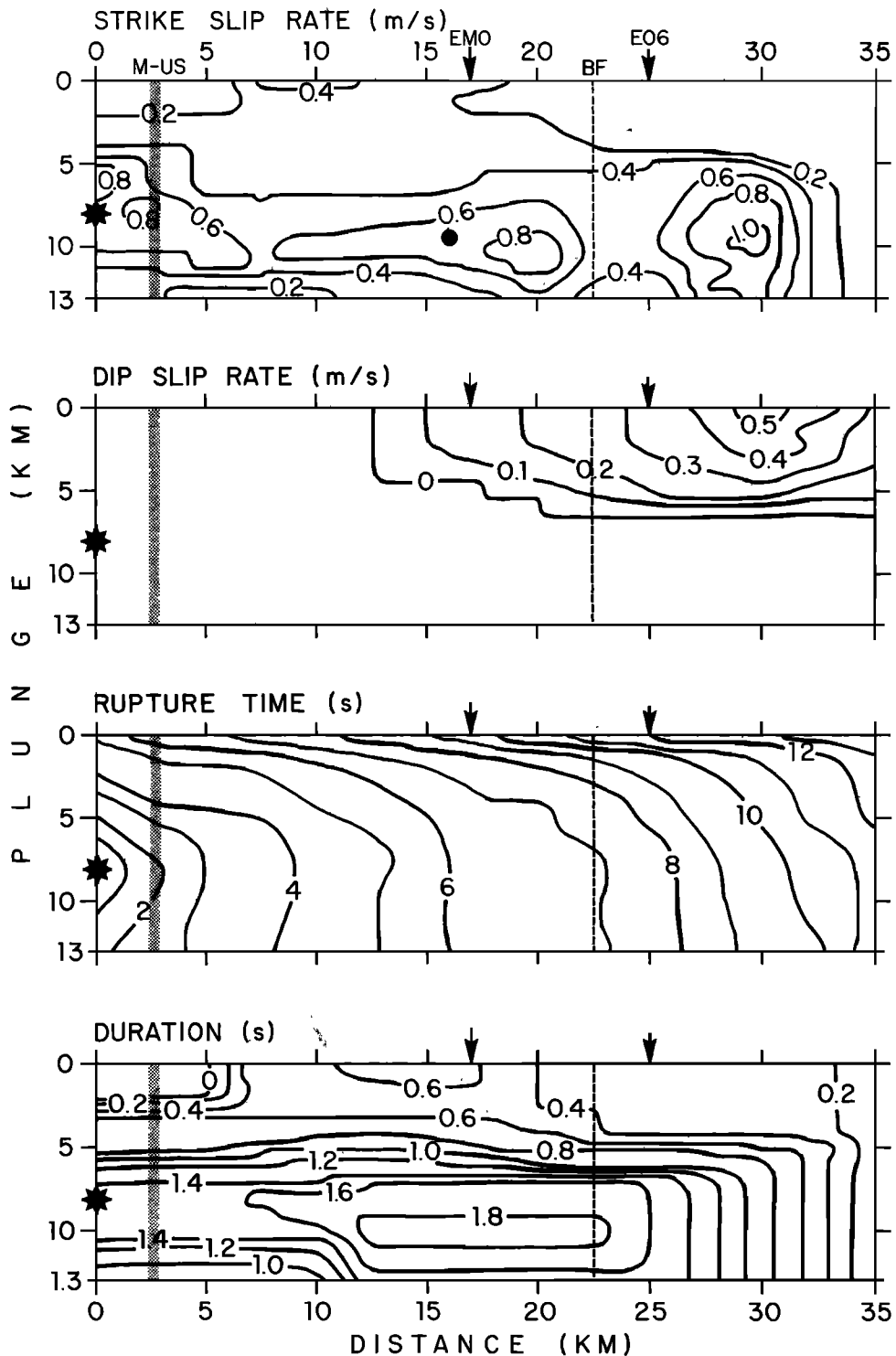


Fig. 6. Contours of the slip rate parameters on the Imperial fault plane. Distances are measured along strike starting at the epicenter. The hypocenter is shown by the star. The down dip coordinate starts at the earth's surface. The Imperial fault plane dips 80° NE. For reference, the locations of the Mexico-U.S. border (M-US), Meloland (EMO), E06, and the intersection of the Brawley fault (BF) are shown. The solid circle indicates the hypocenter of the 2319:35 UT aftershock.

1981] to be compared with the data. We defined the four slip rate parameters on a 182-point grid which had 1-km spacing in the downdip direction and 2.5-km spacing along strike. Depending on the local shear wave velocity at a given depth, Spudich's [1981] method interpolates on the array of input parameters to guarantee a minimum of six samples per wavelength for a given frequency. In our particular model-

ing, we specified a minimum of eight points per wavelength. At first we used only the data of E03, E05, E06, E07, E08, E11, HVP, and BCR to constrain our selection of $\dot{s}(x, t, T, \tau)$. Later, EMO was added and much later in our modeling E04. Thus the synthetics at E01, E02, EDA, E10, E12, and E13 are predicted from the faulting model determined by the other stations.

Table 2. Values of Rupture Times on the Imperial Fault

Depth, km	Distance, km														
	0.0	2.5	5.0	7.5	10.0	12.5	15.0	17.5	20.0	22.5	25.0	27.5	30.0	32.5	35.0
0.0	5.5	6.3	6.6	7.2	7.8	8.4	8.9	9.8	10.6	11.3	12.0	12.3	12.6	13.3	13.9
1.0	4.5	5.2	5.2	5.7	6.5	7.0	7.6	8.0	8.5	9.1	9.8	10.5	11.1	11.7	12.4
2.0	4.3	4.9	4.8	5.0	5.6	6.2	6.8	7.4	7.8	8.3	9.3	10.0	10.7	11.6	12.3
3.0	3.5	4.5	4.6	4.8	5.5	6.0	6.4	7.1	7.3	7.9	8.8	9.6	10.4	11.3	12.3
4.0	2.6	3.9	4.2	4.4	5.1	5.6	6.2	6.9	7.0	7.7	8.4	9.4	10.1	11.5	12.3
5.0	1.9	3.2	3.5	3.9	4.7	5.1	5.9	6.6	6.9	7.5	8.3	9.4	10.4	11.3	12.1
6.0	1.2	2.5	3.2	3.8	4.4	5.0	5.9	6.6	6.8	7.0	7.6	9.0	9.8	10.6	11.4
7.0	0.4	2.0	3.1	3.7	4.3	4.9	5.8	6.4	6.7	6.9	7.5	8.8	9.7	10.5	11.3
8.0	0.0	1.7	3.0	3.6	4.3	4.9	5.7	6.3	6.6	6.9	7.4	8.7	9.6	10.4	11.2
9.0	0.4	2.0	3.1	3.7	4.3	4.9	5.8	6.3	6.6	6.8	7.6	8.8	9.7	10.4	11.2
10.0	0.9	2.2	3.2	3.7	4.4	4.9	5.9	6.3	6.7	7.0	7.4	8.8	9.6	10.4	11.3
11.0	1.3	2.4	3.3	3.8	4.4	4.9	5.9	6.3	6.6	6.8	7.4	8.7	9.5	10.3	11.2
12.0	1.6	2.6	3.3	3.9	4.4	4.9	5.9	6.2	6.6	6.8	7.4	8.6	9.5	10.2	11.0
13.0	1.8	2.7	3.4	3.9	4.4	4.9	5.8	6.2	6.5	6.7	7.3	8.6	9.4	10.2	11.0

Rupture times have been rounded to the nearest tenth of a second.

Our choice of the stations used to constrain the faulting model was not random. If one takes a careful look at the data, especially the horizontal components (Figures 3 and 4), it is easy to see that there are certain pulse shapes common to different groups of stations. For example, the pulse shapes on the 323° component of HVP, E03, and E02 are quite similar. Of course, there is the obvious similarity of 53° pulse shapes at E04, E05, E06, and E07. We felt that if we could determine the pulse shapes of one or two members of a group, the others might be well predicted. Another criterion was the amplitude of different pulses. The coherent pulse shapes are also associated with the maximum amplitude at a given station. We were not overly concerned with fitting late arriving energy since the further in time we compute the synthetics, the more pronounced become the errors resulting from the errors in the assumed velocity model. However, we could not ignore the amplitudes of the first arriving energy. Even low passed, the particle velocity at E06 and E07 exceeds 0.8 m/s. Though the amplitudes decrease for stations farther from the fault, there is a rate of decrease that is important, so amplitudes at more distant stations like E03 cannot be ignored. Even though the 53° components at E06 and E07 are similar in shape and amplitude, the 323° components are not. Equally important is the fact that E06 and E07 have any significant amplitude at all on the 323° component considering how nearly nodal these stations are for such motion. The final major consideration was geographical location. Bond's Corner (BCR) has small amplitudes on both horizontals, but it is the U.S. station closest to the epicenter; Meloland (EMO) is the station between the epicenter and the array stations and close to the fault trace, and where possible we tried to pair up stations east and west of the fault (e.g., E03–E11, E05–E08, and E06–E07). Although stations like Brawley Airport (BRA), Parachute Test Site (PTS), and Westmorland (WSM) might have provided more resolution of faulting on the Brawley and Imperial faults, computational costs prevented us from considering stations more than 35 km from the epicenter.

We gave no priority to fitting the vertical component of motion. For high frequencies it is probably the most important component of motion and the least readily explained in terms of simple fault dynamics [Archuleta, 1982b]. We felt that if we could match the horizontal components, the

primary low-frequency motion would be understood and the faulting model would serve as the basis for analysis of the high-frequency pulses. The verticals are simply predictions of the model.

Imperial Fault

The spatial distributions of the four slip rate parameters (strike-slip rate amplitude $\dot{s}_1(x)$, dip-slip rate amplitude $\dot{s}_2(x)$, a rupture time $T(x)$ from which a rupture velocity is derived, and duration $\tau(x)$) are shown in Figure 6. For reference, stations E06 and E07 are at 24.9 km along strike, EM0 at 16.9 km, and Bonds Corner at 3.5 km (Figure 1).

Strike-slip rate. The most obvious feature of the strike-slip rate amplitude is the concentration of the largest amplitudes at depths greater than 5 km. This corresponds to the earlier results of Hartzell and Helmberger [1982], Olson and Apse [1982], and Archuleta [1982b]. The contours also show three regions on the fault where the slip rate is larger than in the surrounding area: Near the hypocenter the slip rate maximum is about 0.82 m/s; at 20 km from the hypocenter and a depth of 11 km the maximum is 0.94 m/s; and at 30 km and a depth of 9 km the largest slip rate is 1.05 m/s on the fault. One could argue that the presence of slip rate concentrations looks like the result of Hartzell and Helmberger [1982], but the amplitudes shown in Figure 6 are 2.5 times smaller and the locations are significantly different. We have tailored the strike-slip rate amplitude combined with the duration, discussed below, to approximate the slip distribution observed at the earth's surface [Sharp et al., 1982]. Because of the low shear modulus and the slow velocity of rupture in the sediments, the near-surface slip rate contributes very little to the radiation. Our modeling efforts imply that the surface measurements provided little constraint on the strike-slip rate parameters. The slip rate is generally quite small for depths less than 5 km. This feature is substantially different from the other faulting models for this earthquake. We were forced to use a small slip rate in the sediments in order to keep small the free surface reflected phases sS and SS . This phase which arrives about 6 s after S can easily be seen in the data and synthetics on the 53° component of motion at stations E04, E05, E06, E07, and E08.

Dip-slip rate. The spatial distribution of the dip-slip rate

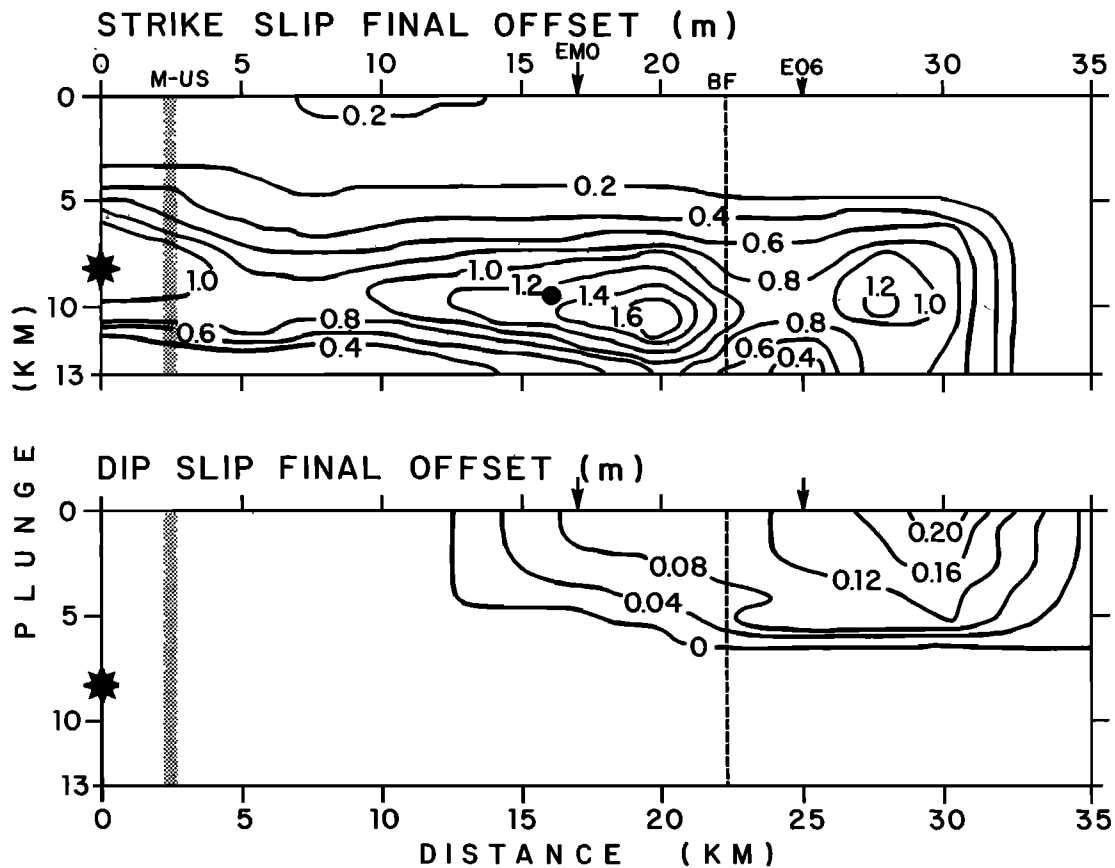


Fig. 7. Contours of the static strike-slip and dip-slip offsets on the Imperial fault plane. See caption of Figure 6 for description of fault plane and annotation. Seismic moment for the Imperial fault is 6.4×10^{18} N m; maximum slip is 1.78 m.

amplitudes complements the strike-slip rate. The distribution coincides with observed surface measurements. The maximum dip-slip rate of 0.55 m/s occurs about 30 km from the epicenter and rapidly decreases to zero at about 6 km depth. Because the dip-slip rate is confined to the sediments where the shear modulus is small and the rupture front arrives later, the radiation due to the dip-slip component of slip rate is small and arrives mostly after the direct *S* waves.

Duration. The duration grossly resembles the distribution of the strike-slip rate amplitude, though the duration is smoother. The duration shows a broad region where it is greater than or equal to 1.5 s with a maximum duration of 1.9 s in the 12 to 22-km range. The duration values can be changed by a couple of tenths of seconds without seriously affecting the synthetics, but they cannot be varied by a full second. The maximum duration of 1.9 s is less than the time for a shear wave to travel half the width of the fault plane. The duration is not controlled by the entire width of the fault plane [Archuleta and Day, 1980; Day, 1982a] but a smaller length scale. This smaller length scale may result from the elastic velocities varying with depth. The maximum duration of 1.9 s is much shorter than the time for the rupture to reach the end of the fault, approximately 11 s, and thus our model of the Imperial Valley earthquake does not support the length scaling hypothesis of Scholz [1982]. Although we tried durations that were constant everywhere on the fault, no constant value would generate pulse widths consistent with all the data. Durations much smaller than 1 s are not well

resolved by our low passed data. Since we are considering frequencies of 0–1.0 Hz, the slip rate function will approximate a delta function for all durations much less than 1.0 s.

Rupture time. The most unexpected feature of the faulting model is the spatial distribution of the rupture time. The contour lines of rupture time show the position of the rupture front at equal 1-s intervals of time. Large areas between two successive time intervals indicate a fast rupture velocity, and small regions indicate a slow rupture velocity. Unfortunately, the contours do not reveal the complete picture. In Table 2 the actual values of the rupture time used to compute the synthetics are given. Special care must be taken in determining average local rupture velocities near the region, 17.5–22.5 km, where the rupture abruptly accelerates. The basic character of the rupture velocity is observed at the hypocentral depth of 8 km. For reference, the *S* wave velocity is 3.25 km/s. The rupture starts slowly at about 1.5 km/s and continuously accelerates to about 4 km/s at 10 km. From 10 to 17.5 km, the rupture velocity is nearly constant. Near 17.5 km the rupture abruptly accelerates to 9.8 km/s. The rupture rapidly decelerates in the range 22.5–27.5 km where the average rupture velocity is 1.9 km/s. Around 27.5 km the rupture velocity again accelerates giving an average velocity of 3.0 km/s for the final 7.5 km of faulting. The overall average rupture velocity is 3.1 km/s, which is 0.94 times the local shear wave velocity. In places where the local rupture velocity exceeds the *P* wave speed, the rupture process is causal since the average rupture velocity, distance from

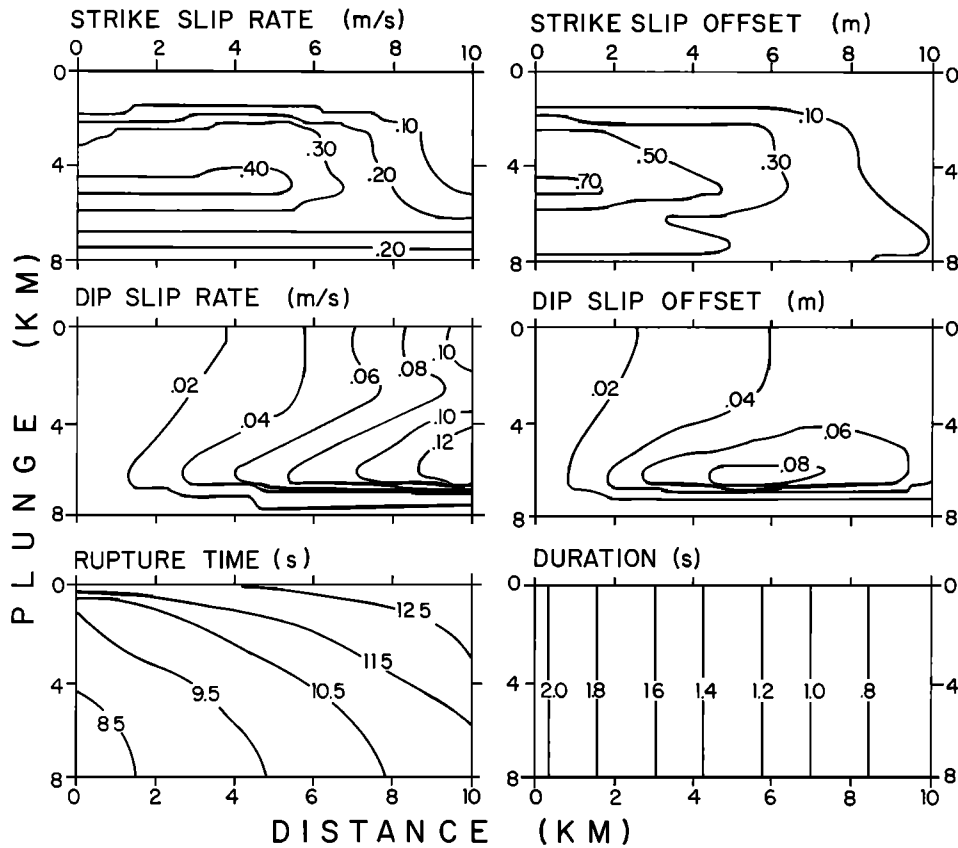


Fig. 8. Contours of slip rate and slip parameters on the Brawley fault plane. The origin for the Brawley fault plane is its intersection with the Imperial fault. The Brawley fault is a vertical plane 10 km long and 8 km deep. Seismic moment for the Brawley fault is 2.7×10^{17} N m.

hypocenter divided by time after origin, is still less than the P wave speed. Areas of locally fast rupture are simply regions where the stress was relaxed nearly simultaneously. Suppose that every point in an area is close to failure. Further suppose that the point farthest from the hypocenter fails at precisely the time at which the rupture from the hypocenter reaches this area. The rupture from the far side of this area will be propagating toward the rupture from the hypocenter. Even though both ruptures may have speeds less than the S wave speed, the simple division of Δx by Δt gives a local rupture velocity exceeding V_s and possibly V_p .

Although our distribution of rupture velocity is defined in more detail, its general character is quite similar to the rupture velocity of *Olson and Apsel's* [1982] model. Our average rupture velocity between 10 and 30 km is less than 4.0 km/s, however. Having a rupture velocity that exceeds the local shear wave speed and in one instance the local compressional speed may be unusual, but it is not unphysical [Burrige, 1973; Andrews, 1976; Das and Aki, 1977; Das, 1981; Day, 1982b]. In fact, this highly variable rupture velocity may provide information about the stresses acting on the fault during the rupture [Das and Aki, 1977; Virieux and Madariaga, 1982; Day, 1982b].

There is an important correlation between the rupture velocity and slip rate amplitude in this model. With the exception of the region near the hypocenter, where the rupture velocity is fast, the slip rate amplitude is high; in

areas where the rupture is slow, the slip rate amplitude decreases. This correlation is strongest in the 10- to 30-km range for depths greater than 5 km. A similar correlation is found in *Day's* [1982b] results.

Static slip. The distribution of the static strike-slip and dip-slip amplitudes on the Imperial fault is shown in Figure 7. The static slip is simply the product of slip rate amplitude and the duration. Overall, the static slip distribution is similar to the slip rate distribution. The maximum strike-slip offset of 1.78 m occurs at 20 km and a depth of 10 km. The average strike-slip offset for the entire fault is 0.41 m; by coincidence this is exactly the average offset of the surface measurements [Archuleta, 1982b]. The maximum dip-slip offset of 0.22 m occurs at the surface. The seismic moment for the Imperial fault is 6.4×10^{18} N m; 98.5% comes from the strike-slip offset.

The amount of right-lateral slip is consistent with strain accumulation since 1940. If one integrates an aseismic strain of $59 \mu\text{rad}$ (average of triangles S_1 and S_2 [Snay et al., 1982]) over a distance equal to the depth of faulting, 13 km, the tectonically accumulated slip since 1940 is 1.54 m. In an earlier paper [Archuleta, 1982b] we erred in our analysis of the strain data and incorrectly concluded that the accumulated strain since 1940 could not account for the coseismic strain release of the 1979 main shock. In fact, the analysis by *Snay et al.* [1982] shows that the coseismic strain release is only 60% of the tectonically accumulated strain since 1940.

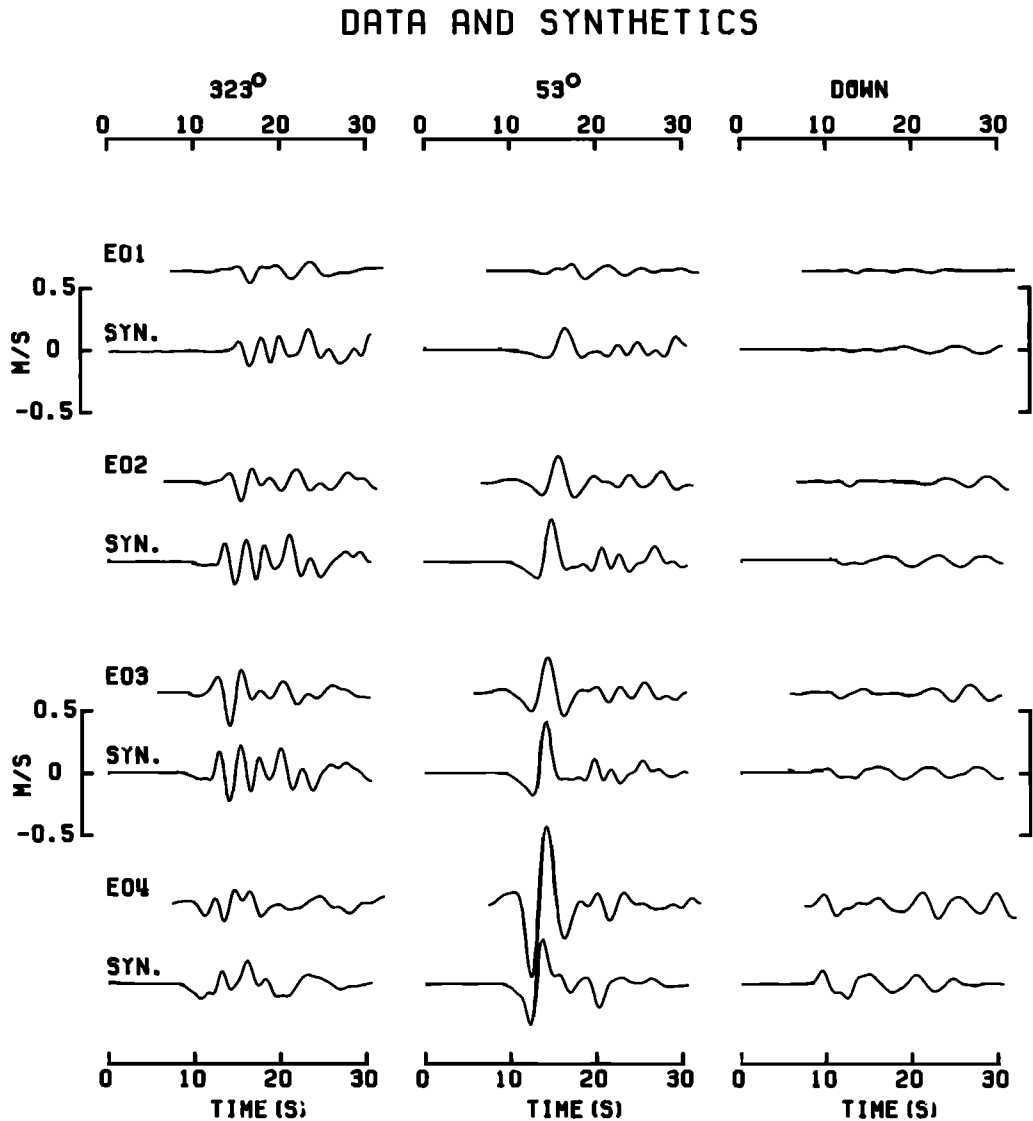


Fig. 9a. Comparison of three components of synthetic particle velocity time histories with the data at stations E01, E02, E03, and E04. All components are plotted to the same amplitude scale. For stations where absolute time was available (E01, E02, and E04), the synthetics have been aligned accordingly; for stations where absolute time was not available (E03), the synthetics have been shifted for the best fit. This shift is generally less than 1.0 s from the trigger time of nearby stations. Stations E01 and E02 were not used to constrain the faulting model.

Brawley Fault

Besides the highly variable rupture velocity on the Imperial fault, the next most unusual aspect was faulting on the Brawley fault zone, Figure 1 [Sharp, 1976]. The surface measurements of Sharp *et al.* [1982] and creep measurements by Cohn *et al.* [1982] suggested that slip occurred at or near the time that the Imperial fault ruptured. The surface measurements showed small dip-slip and strike-slip offset, and the length of faulting was only about 10 km. Compared to the Imperial fault, any faulting on the Brawley fault might be assumed to be insignificant. With that assumption we tried almost 200 faulting models for the Imperial fault and failed to model the 323° component of motion at stations E06 and E07. The amplitude of the 323° component at E06 is almost half the amplitude of the 53° component which is the largest of all the data.

Including the Brawley fault was the last major perturbation to the faulting model. There are few constraints on the

Brawley fault. First, the geometry of the Brawley fault in this area is not well determined. Although the surface breaks are not continuous (Figure 1), they trend almost due north, which we assumed to be the strike. To model the Brawley fault zone, we assumed a vertical fault of 10-km length that begins at its intersection with the Imperial fault, 115°28.65'W, 32°48.90'N, about 22.3 km northwest of the epicenter. Aftershock locations by Boore and Fletcher [1982], seismicity in 1976 near the northern end of this 10-km break [Johnson and Hadley, 1976], and seismicity in 1977 at the intersection of the Brawley fault with the Imperial fault [Johnson and Hill, 1982] indicate a maximum seismogenic depth of about 8 km. After trying about 30 models of various slip rate parameters, some with dips of 80° W and some with depths down to 10 km, we decided on a faulting model shown in Figure 8. The second constraint is that slip on the Brawley fault must produce particle motion that complements the motion generated by the Imperial fault. This constraint is totally dependent on the model of the Imperial

DATA AND SYNTHETICS

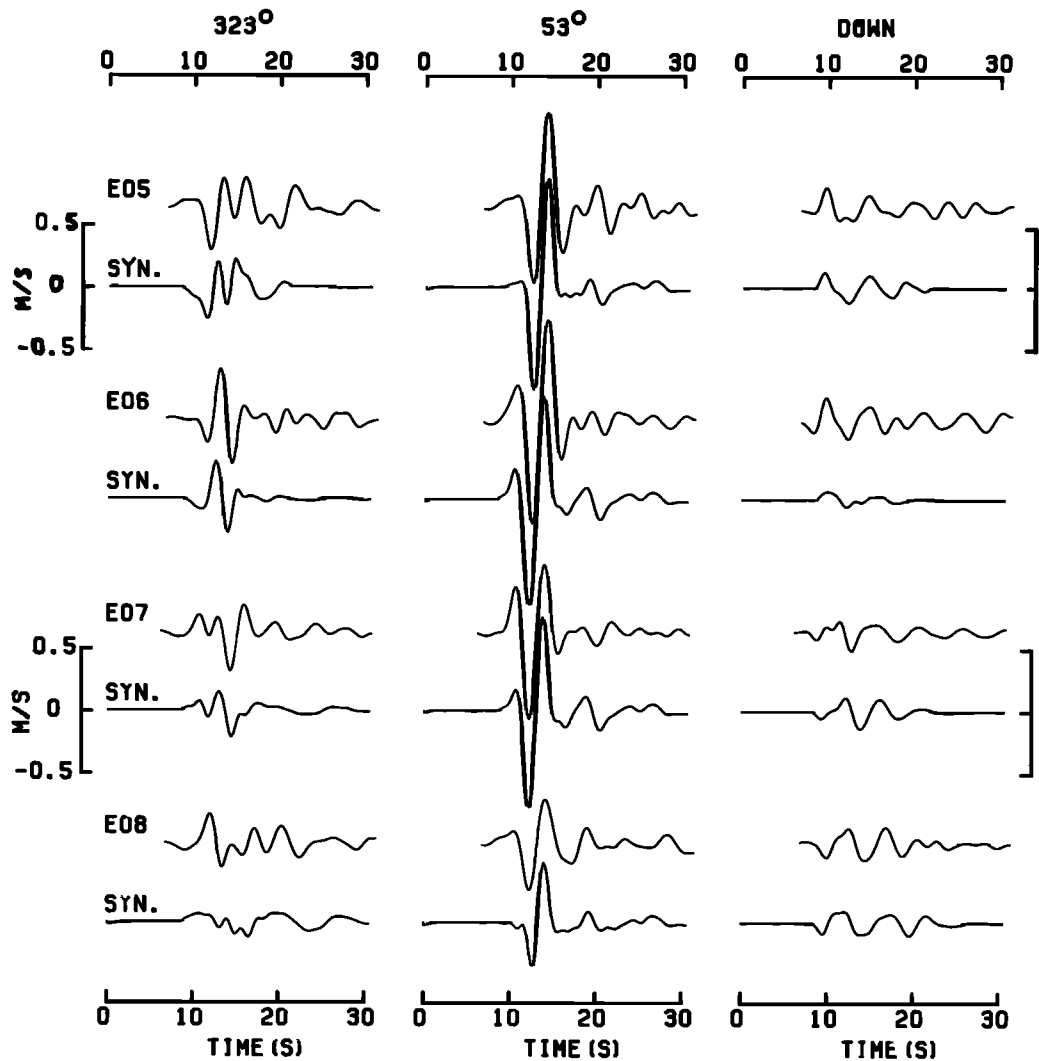


Fig. 9b. Comparison of synthetic particle velocities and data at stations E05, E06, E07, and E08. No absolute time at E07. See caption of Figure 9a for further explanations.

fault; as such, it often created a dilemma as to which faulting model should be perturbed to produce a better fit.

Although the surface measurements [Sharp *et al.*, 1982] showed vertical motion, east side up, of the order of 0.10–0.15 m, the primary motion at depth is right-lateral strike slip. The strike-slip rate is generally confined to a narrow region between 2- and 6-km depth with the amplitudes tapering off as one moves northward on the Brawley fault. The maximum strike-slip rate is 0.44 m/s at a depth of 4 km. The dip-slip rate distribution is considerably different from the strike-slip rate distribution. The dip-slip rate is rather uniform in depth but increases from south to north. The maximum dip-slip amplitude of 0.14 m/s is considerably smaller than that for the strike-slip component. The duration is not well constrained. The two features which are required are the general decrease in duration as one moves from south to north along the Brawley fault and the general length of the duration. The rupture time is a smooth function on the fault and is well approximated by a constant rupture velocity 0.95 times the local shear wave velocity. On the basis of the

superposition of the Brawley fault synthetics with those of the Imperial fault, the Brawley fault started rupturing about 1 s after the rupture front on the Imperial fault had passed the intersection of the two faults. Note that the intersection of the two faults is the point at which the rupture velocity on the Imperial fault abruptly decelerates (Figure 6). The static strike-slip component is largest near the southern end of the Brawley fault with a small area having slip values near 0.8 m. The average strike-slip offset is 0.36 m. The dip-slip static offset is substantially less than the strike slip. Although the dip-slip rate grew progressively larger as one moved south to north on the Brawley fault, that is not true of the static dip-slip distribution. At the surface the predicted coseismic dip-slip offset is about 0.06 m. The seismic moment of the Brawley fault is 2.7×10^{17} N m.

SYNTHETIC SEISMOGRAMS

Synthetic particle velocity time histories computed from the combined faulting models for the Imperial and Brawley

DATA AND SYNTHETICS

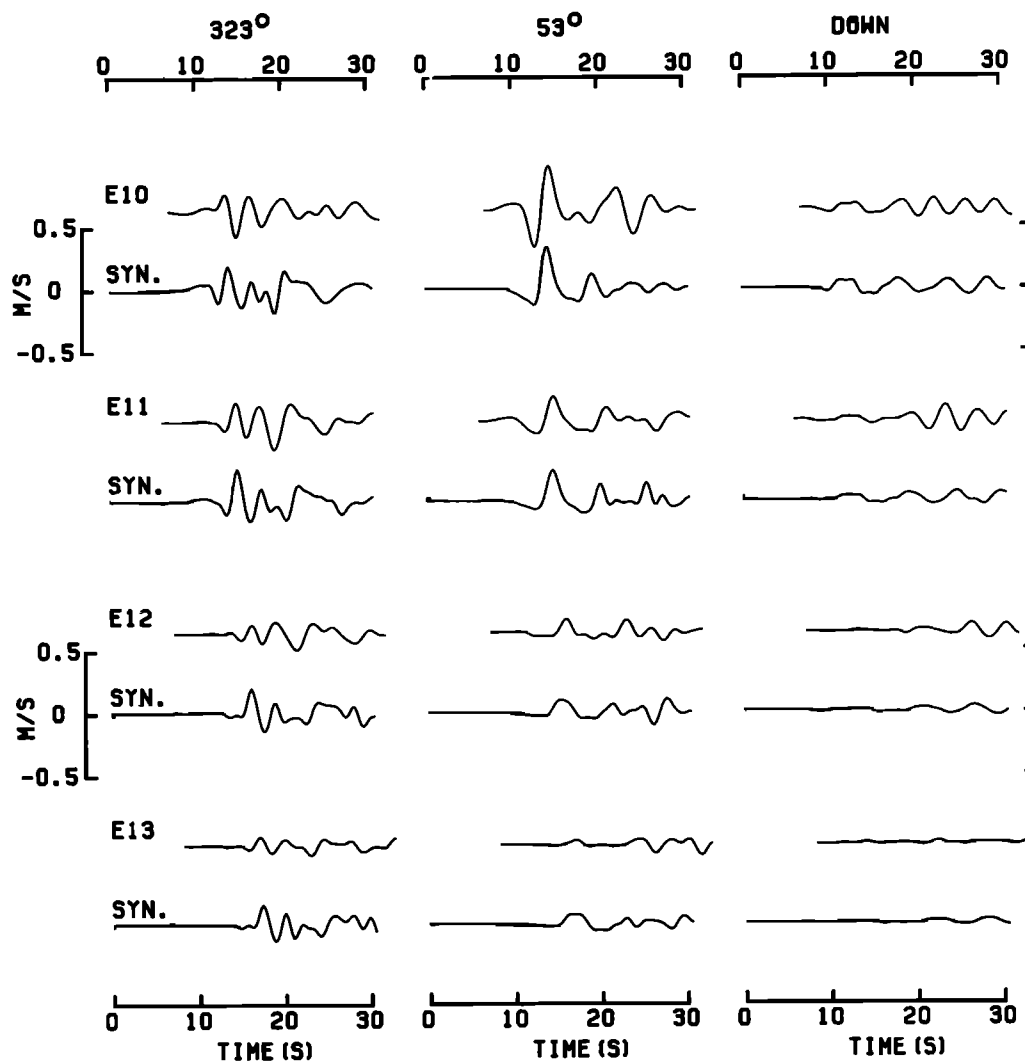


Fig. 9c. Comparison of synthetic particle velocities and data at stations E10, E11, E12, and E13. No absolute time at E10. Stations E10, E12, and E13 were not used to constrain the faulting model. See caption of Figure 9a for further explanations.

faults are compared with 48 components of data in Figures 9a-9d. The time scale for the data and synthetics is seconds after origin time; the data traces have been aligned according to the trigger time when absolute time was available. For those stations not having absolute time, we shifted the data traces for the best alignment with the synthetics. All components at a given station were shifted equally and by less than 1 s compared to the trigger time at nearby stations which did have absolute time. All amplitudes are shown to the same scale. As mentioned earlier, our primary efforts were directed toward matching the horizontal components at 10 stations: E03, E04, E05, E06, E07, E08, E11, HVP, EMO and BCR. The synthetic seismograms for the vertical components and the other stations are predictions of the model.

Before examining the synthetic seismograms, we want to discuss for a moment goodness of fit in general terms. To our knowledge, there is no universal method for assigning a quantitative measure to the goodness of fit between synthetics and data. There are techniques, for example, least squares and cross correlation, that provide some estimate of

the misfit. However, there are many circumstances when these methods would fail to give an accurate picture of the misfit. For example, suppose a synthetic seismogram, assumed to be oscillatory, exactly overlays a data trace except that the synthetic is slightly phase shifted. A least squares estimate of the misfit would hardly be representative, especially if one considers that the phase shift may be a consequence of a slightly incorrect velocity model. Within what might be considered tolerable errors due to assumptions about the fault plane, faulting parameters, or the structure of the medium, the fit would be considered excellent. The operational phrase is "tolerable errors." Since the probability distribution function for errors in the synthetic seismograms is unknown, it is not possible to be rigorous in assigning measures of misfit between synthetic seismograms and data. We are left with visual comparison and geophysical judgment. Although this has some drawbacks, it also has some merit. A positive aspect is that one's eyes are not easily misled when there is a straightforward comparison of synthetics and data. Since all the amplitudes and phases will

DATA AND SYNTHETICS

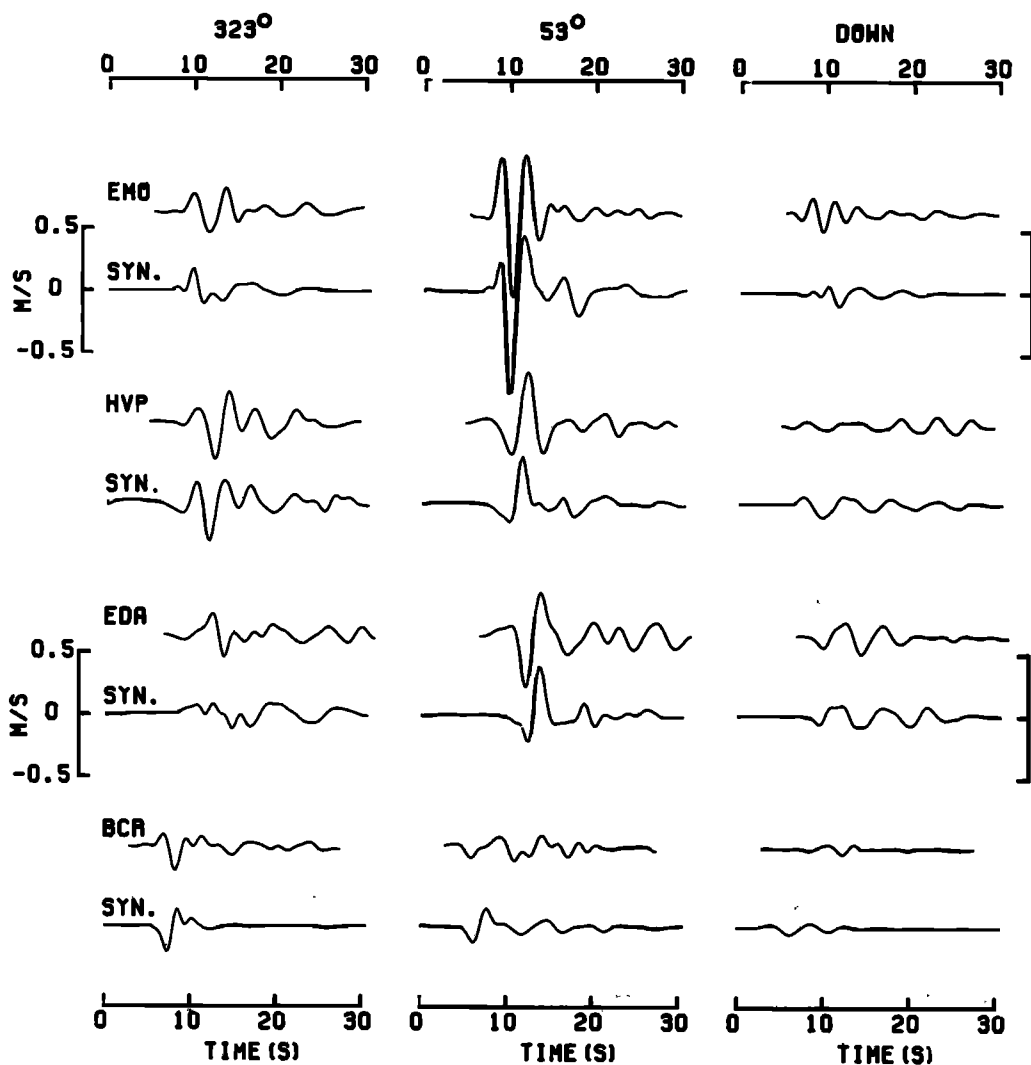


Fig. 9d. Comparison of synthetic particle velocities and data at stations EM0, HVP, EDA, and BCR. No absolute time at EDA and HVP. Station EDA was not used to constrain the faulting model. See caption of Figure 9a for further explanations.

not be matched perfectly, it is important to have some idea about which pieces of the data are more important than others. To the degree that one can examine synthetics generated by different models, one can assimilate a quasi-quantitative feeling about the goodness of fit.

First, we consider the general aspects of the synthetic seismograms that agree with the data. The percentage error between the maximum peak-to-peak amplitude in the *S* wave packet of the data and the corresponding peak-to-peak amplitude in the synthetics is plotted in Figure 10. The percentage error is generally less than 50% and often less than 30% except for stations farthest from the fault. Although we have been rigorous in making sure we are comparing the amplitudes from the same phases, the results should be taken in conjunction with the visual comparisons in Figures 9a-9d. In fact, we do not assign an error to the 323° component at E04 and E08 because it is not clear what amplitudes should be compared. In a gross sense the amplitudes of the synthetics at these two stations are roughly equal to the data, but the particular phase in the synthetic is

so ill-defined that we have no confidence in selecting an amplitude. The peak amplitudes are not the only measure of agreement. The correspondence of the phases is equally important. For the *S* wave packet the phases of the synthetics agree with the data within 0.5 s or less. Although any particular component of synthetic particle velocity may not agree well with the data, we think one should consider the overall fit among different components at a particular station as well as the fit from station to station.

Figure 9a shows comparisons of synthetics and data for stations E01 (26.4, 21.6), E02 (24.9, 15.3), E03 (24.0, 12.6), and E04 (24.1, 6.9), where the (y_1 , y_2) coordinates are measured with respect to the Imperial fault origin shown in Figure 1. The data are always shown as the upper trace of each pair and are labeled with the station name. The synthetics at E01 and E02 were predicted by the model. The most disconcerting misfit occurs on the 323° component after the arrival of the direct *S* waves. For example, at E03 the synthetic (323°) tracks the data very well through the first peak-trough-peak cycle. However, the synthetic continues

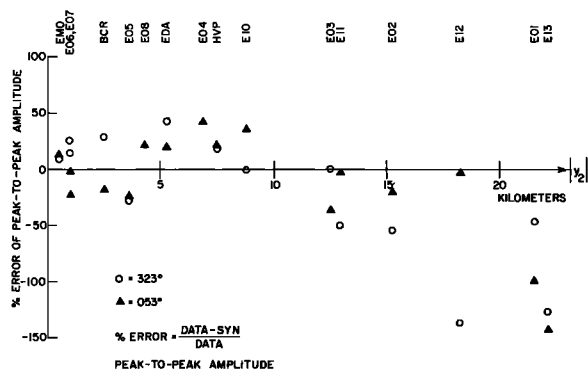


Fig. 10. The percentage error between the maximum peak-to-peak amplitude in the data and the corresponding peak-to-peak amplitude in the synthetics for the horizontal components in Figures 9a–9d. Because we cannot identify a corresponding phase in the 323° synthetic at E04 and E08, no error is plotted. Excepting the stations farthest from the fault, the percentage error is generally less than 50% and often less than 30%.

with a substantial trough-peak motion that is not as amplified in the data. The strength of this phase detracts from the fit between the synthetics and the data for the 323° component at E01, E02, and E03. In many ways the synthetics at E04 represent our worst fit between all the synthetics and data. Because the synthetics at E03 and E05 agree relatively well with the data, the misfit at E04 is somewhat surprising. We know from other fault models we tried that we can trade off the fit on the 323° component with that on the 53° component. The shoulder on the 53° component at about 15 s comes from the Brawley fault, an indication that the model of the Brawley fault could use more refinement. Although one cannot see much detail in the vertical components at this scale, the fact that the synthetics also have small amplitudes is encouraging.

Figure 9b shows the data and synthetics at E05 (25.2, 3.6), E06 (24.9, 1.0), E07 (24.9, -1.0), and E08 (24.9, -4.3). Except for the 323° component at E08, the synthetics fit the data reasonably well. There are four features to note. First is the 323° component at E06 and E07. Although by theory this component should be practically nodal for a rupture on the Imperial fault, it clearly is not, nor is it antisymmetric even though from the location of E06 and E07 it should be nearly so. This occurs because this component is influenced by rupture on the Brawley fault, which is discussed in a later section. The second element is the vertical fit. Although it is far from perfect, the synthetics and data at E05, E07, and E08 show a definite similarity. In particular, the first energy arriving at about 9 s is associated with the large-amplitude vertical accelerations. The source of this energy is the fault area on which the local rupture velocity is extremely fast and variable. The third aspect is that on the 53° component the synthetics show the same amplitude and double-sided character as the data. The strike-slip rate concentrations have amplitudes about 0.8 m/s. Since geometrical spreading attenuates the amplitude by $1/R$, the fact that the low-passed particle velocities have maximum amplitudes about 0.8 m/s suggests that there is a considerable amount of constructive interference of waves from different parts of the fault. The last feature to note is the small pulse in the data, arriving at about 18–20 s on the 53° component. This pulse, observable in the synthetics, is SS. The amplitude of this pulse is

strongly dependent on the slip-rate amplitude in the sediments. To match the synthetic SS pulse with the data requires the model to have small slip-rate amplitudes at depths shallower than 5 km.

The data and synthetics for E10 (24.1, -8.8), E11 (23.1, -13.0), E12 (22.5, -18.3), and E13 (24.1, -22.2) are shown in Figure 9c. Of this group, only the data at E11 were used in constraining the faulting model; the synthetics at E10, E12, and E13 are predictions. The basic pulse shapes of the data are reproduced by the synthetics even on the vertical; however, the amplitudes of these synthetics are too large, particularly at E12 and E13. Station E13 is located in and station E12 is located near the region where the sediment thickness in the Imperial Valley is rapidly decreasing [Kohler and Fuis, 1983]. If the sediments were more rigid than assumed in our model, the synthetics would be larger than the data.

The final four stations for which we computed synthetics are the free-field site at Meloland overpass, EMO (16.9, -0.5); Holtville Post Office, HVP (16.3, 7.5); the SMA-1 at the El Central differential array, EDA (23.9, -5.3); and Bonds Corner, BCR (3.5, 2.5). Because these stations are so geographically diverse, they do not constitute a group in the same sense as the preceding three figures. Meloland is not well fit on either the 323° or vertical component. In our trial and error modeling, we found that almost no perturbation could produce the waveforms on the 323° and vertical components. The part of the Imperial fault closest to the station has the greatest influence on the 323° and vertical components; the 53° component has contributed that result from integrating the slip-rate contributions from the entire fault. Of all the areas on the Imperial fault that show any surficial en echelon fault traces, the most obvious place is immediately adjacent to the Meloland station. At Meloland the Imperial fault shows two distinct surface traces [Sharp *et al.*, 1982, Plate 1]. Holtville is almost directly across the Imperial fault from Meloland but 7.5 km off the strike. The 323° component is well matched; the 53° synthetic is similar to the data, but the main pulse is too narrow; the vertical synthetic has almost the same waveform as the data, but its amplitude is too large. Station EDA is between E08 and E10. EDA has the same character of misfit as does E08 and E04. The last station is Bonds Corner. Since we did not use the Mexican stations, Bonds Corner has the greatest influence in determining the behavior of the rupture near the hypocenter. The most difficult feature of the data to match at Bonds Corner is the 2-s time difference between the clear pulse on the 323° component and the small first motion on the 53° component. The first motion on the 53° component is due to the faulting in the immediate hypocentral region. To obtain any resemblance to the Bond's Corner record, we needed an initially slow updip rupture with an increase in slip-rate amplitude slightly shallower than the hypocenter. There is a complicated interference between energy arriving from 8- to 10-km depth and that arriving from the 4- to 6-km depth which eliminated the first motion on the 323° synthetic.

In summary, the major discrepancies between the synthetics and the data occur on the 323° component at stations E0A, E08, EDA, and EMO on some of the vertical components and at E01, E12, and E13 on the horizontal. The 323° component of data at E08 and EDA shows a distinctive change in direction from 323° to 143° which is not found in the synthetics. Models that mimic this pulse well tend to

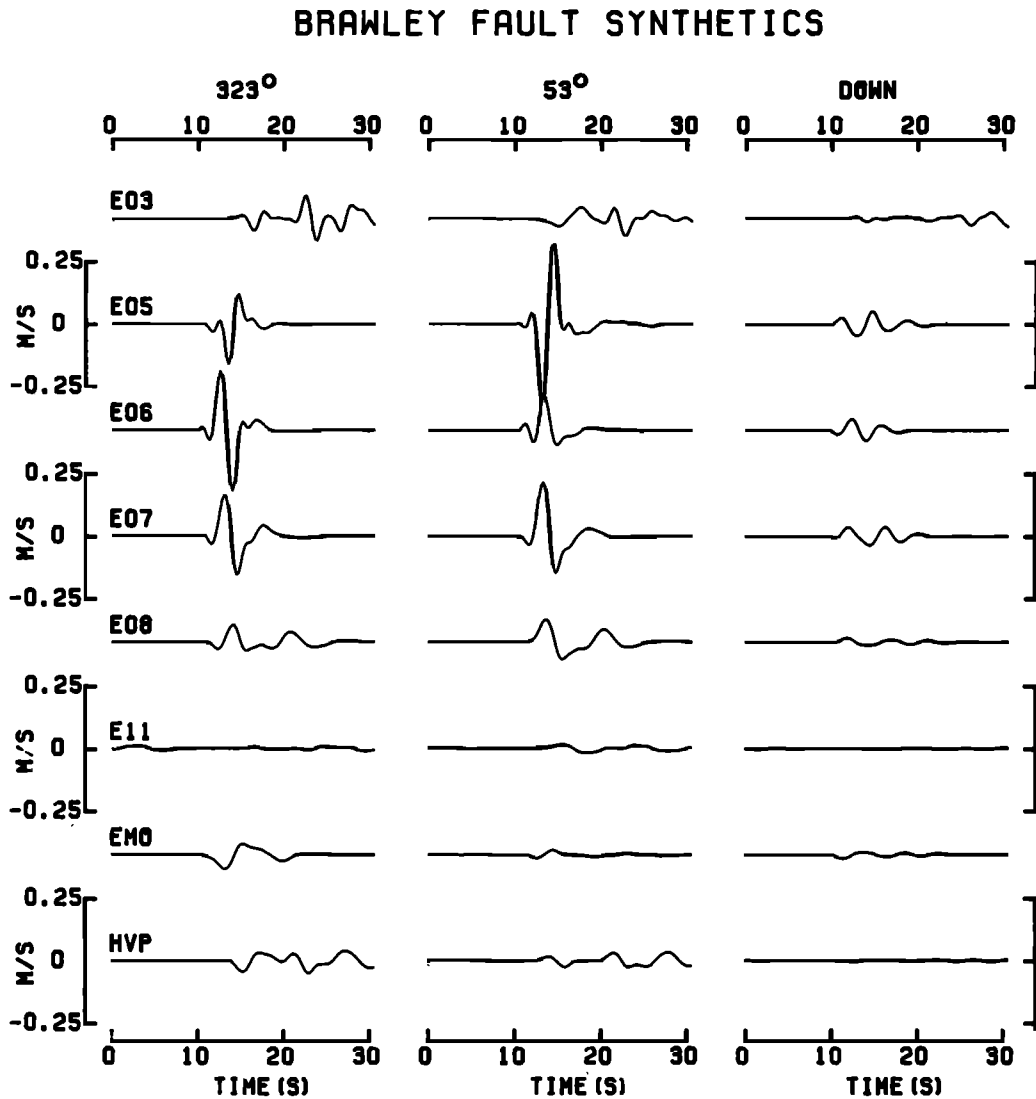


Fig. 11. Representative particle velocity time histories generated by rupture on the Brawley fault. Note how different components at a given station are affected. Also note that station E11 (and, although not shown, E12 and E13) is almost unaffected by the Brawley faulting.

destroy the direct S wave pulse on the 53° component at the same stations. The models that do reproduce the 323° component at E08 have almost all the same features as those shown in Figure 6, but the rupture velocity is slower in the 10- to 20-km range and almost instantaneous in the 17.5–22.5 km range. The fit between the synthetics and the data for the vertical motion is variable. In some cases (e.g., E05, E08) the fit is rather good. The amplitudes and the phases are both good. At stations like E06 and E07 there are suggestions of the observed vertical motion, but the synthetics are not very good fits. Other synthetics like HVP have too much vertical amplitude though the phase is well matched, while EMO has too little amplitude. Many of the stations have no dominant first arrival and low-amplitude surface waves. In these cases the synthetics successfully match the ratio of the amplitude of the body waves with the surface waves. It is very difficult to match the precise phase of short-period surface waves since they require a precise knowledge of the P and S wave velocity structure. The fact that the relative amplitude between the synthetic body waves and surface waves is in

proportion to the observations is encouraging. While the fit between the synthetics and the data is not perfect, the basic character of the faulting model is well defined. In the next sections we describe the features of the data that require the important aspects of the faulting model.

Brawley Fault Contribution

One of the more unusual aspects of the data is the large amplitude of the 323° component at E06 and E07. A more subtle aspect is the amplitude in the 53° direction at E05 and E07 compared to the amplitude in the 233° direction. SH radiation from the fault southeast of the array station will produce particle motion in the 233° direction. If the rupture velocity were always less than the local S wave speed, we would expect the 233° direction to be amplified by directivity (preferential focusing of radiated energy) from the propagating rupture. If this difference between the 53° and 233° amplitudes were due to the spatial distribution of the slip rate on the Imperial fault (e.g., larger slip rate north of the array), E06 would also show the same ratio of amplitudes with the

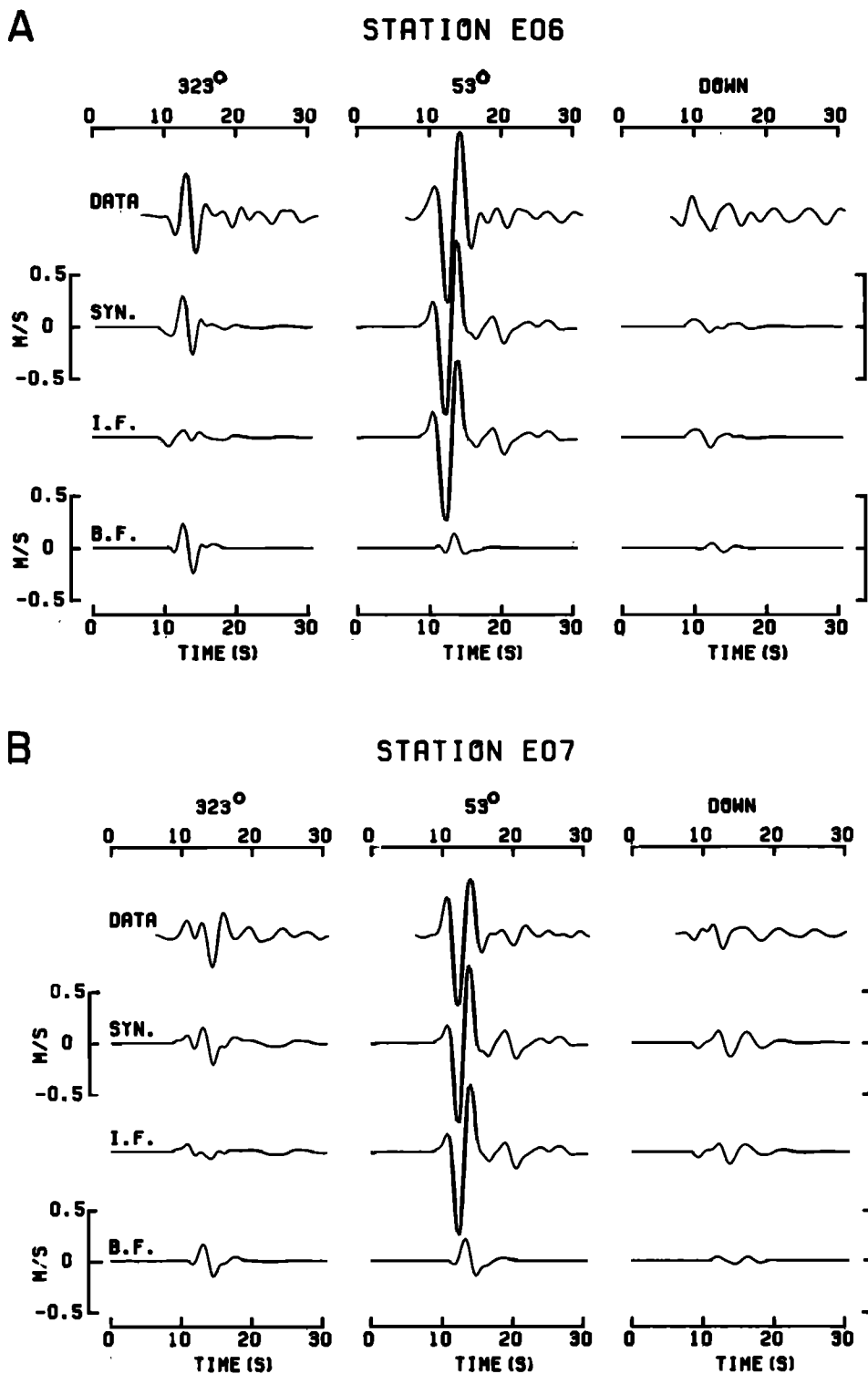


Fig. 12. (a) An example of how the total synthetic at E06 is generated by the combined radiation from the Imperial fault and the Brawley fault. The 323° component is nearly nodal for the Imperial fault but strongly affected by the Brawley fault. The 53° component is dominated by radiation from the Imperial fault. (b) Motion at E07 is generated by the Imperial fault and the Brawley fault. Allowing for the expected antisymmetry, the Imperial fault contributes almost the same motion for the 323° component at E07 as it does for E06. However, it is the Brawley fault's contribution that destroys the expected antisymmetry of the 323° component at E06 and E07. A more subtle effect is the way in which the Brawley fault's contribution subtracts from motion in the 233° direction and adds to the motion in the 53° direction.

amplitude in the 53° direction exceeding the amplitude in the 233° direction. E06 does not show this. These features of the data can be explained by slip on the Brawley fault. Although the Brawley fault contributes only 4% of the total seismic

moment, it has a marked effect on the ground motion of nearby stations (Figure 11). Figure 11 shows most of the stations that were strongly affected by slip on the Brawley fault. Another station that might have recorded significant

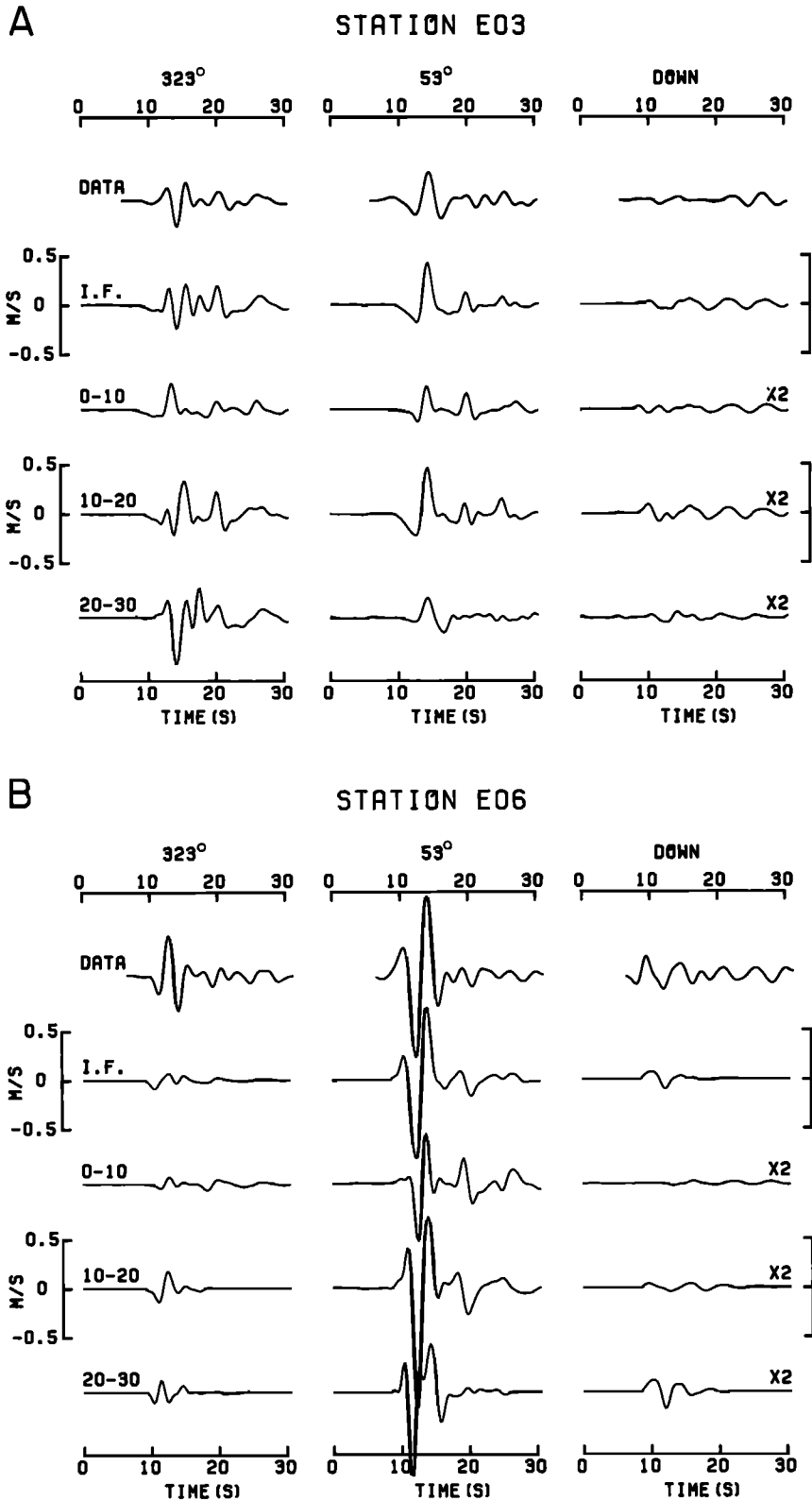


Fig. 13. (a) An example of how three equal fault segments combine to produce the synthetic particle velocity contribution from the Imperial fault at E03. The amplitudes of the synthetics for each segment have been multiplied by 2 indicated by X2 on the right-hand side. The segments are labelled 0-10, 10-20, and 20-30, indicating the distance range measured from the epicenter. The large trough in the 323° total synthetic is primarily due to the contribution of the 20- to 30- km range. (b) Synthetic at E06 is composed of radiation from the same segments. Note how the 10- to 20-km range has the largest contribution to the 53° component's leading trough at E06.

motion from the Brawley fault would be Brawley airport (BRA), which is not included in this study. It is obvious from Figure 11 that the Brawley fault affects the nearby stations differently. For example, at E05 the 53° component is most affected, whereas the 323° component at E06 is most affected.

Having determined that the Brawley fault produced ground motion that complemented the motion from the Imperial fault, we questioned the necessity of having a northeast dip on the Imperial fault. The strike of the Brawley fault immediately destroys the symmetry between stations east and west of the Imperial fault. The Brawley fault does explain the major differences between E06 and E07, but it does not explain the amplitude differences for stations farther from the fault. The motion generated by the Brawley fault is too small and too late at stations like E03 and E11. A northeast dip on the Imperial fault is still required to explain the data.

Figures 12a and 12b illustrate the contribution of the Brawley fault to the total motion at E06 and E07, respectively. The total synthetic is divided into the contributions from the Imperial fault and from the Brawley fault. The most obvious contribution is to the 323° component of motion at E06 and E07. The Imperial fault generates particle velocities that are nearly nodal and reflected images of each other. Because E07 is farther away from the Brawley fault, the contribution to E07 is smaller than that to E06. At E06 (Figure 12a) the particle velocity from the Brawley fault adds to the particle velocity from the Imperial fault, while at E07 (Figure 12b) the particle velocity due to the Imperial fault subtracts from the 323° particle velocity generated by the Brawley fault. This shows why the 323° time history at E07 is not the reflection of the 323° time history at E06. The effect of the Brawley fault on the 53° component of motion is less obvious. At E06 (Figure 12a) the Brawley fault subtracts a little from the motion in the negative direction due to the Imperial fault but adds to the motion in the 53° direction. At E07 the Brawley fault contributes a larger pulse in the 53° direction, and the pulse arrives later. Hence at E07 the Brawley fault subtracts substantially from the particle velocity in the 233° direction while adding to the motion in the 53° direction. It is difficult to say whether the vertical motion from the Brawley fault helps or hinders the fit between synthetic seismograms and data at E06 and E07.

Constraint on Rupture Time

In this section, we examine how different segments of the fault contribute to the total motion at E03 and E06 to see why the rupture time parameter for the Imperial fault has its spatial distribution. We divide the Imperial fault into three equal segments measured from the epicenter: 0–10, 10–20, and 20–30 km and ignore the last 5 km. The synthetic particle velocity time histories from these three segments plus the total synthetic for the Imperial fault are shown in Figures 13a and 13b for E03 and E06, respectively. The amplitudes of the synthetics from the three fault segments have been multiplied by two.

The gross effect of adjusting the rupture time is to move the radiation from these segments individually to a different arrival time. We perturbed the rupture time from a subshear rupture velocity for almost a hundred models. If we fit the amplitudes recorded by stations near the fault, we could generate only very small amplitudes on the 323° component at the more distant stations such as E03. The effect of a

subshear velocity on the segment time histories is to shift the 10- to 20-km and 20- to 30-km time histories to successively later time. Looking at Figure 13a, one can see how the total synthetic will be generated under the assumption of a subshear rupture velocity. The amplitudes in 0–10 km might be adjusted to fit the first motion in the 323° direction, but the obvious trough in the data on the 323° component will have to come from the 10- to 20-km range, which implies large slip rates in this region. The large positive motion (motion in the 323° direction) generated by the 10- to 20-km range will have to be countered by the trough from the 20- to 30-km segment. Large slip rates in the 10- to 20-km range are necessary because with a subshear rupture velocity, the only negative motion (motion in the 143° direction) that can arrive at the correct time relative to the first 10 km (i.e., the origin time) must be associated with the second small trough of the 10- to 20-km synthetic.

There is a severe penalty for adjusting the amplitudes in this way. One has only to look at Figure 13b to see the consequences. The 53° component at E06 is going to change dramatically. Any large increase in the slip rates in the 10- to 20-km range will produce a large trough on the 53° component. Depending on the time shift of the 20- to 30-km range, radiation from the 20- to 30-km segment will either add to the particle velocity in the negative direction, making it even more negative, or it will subtract from the amplitude of the peak in the 53° direction. The net effect is to produce a pulse 2 to 3 times larger in the 233° direction and diminish the pulse in the 53° direction. Instead of nearly symmetric waveform, the 53° component will have a single trough whose amplitude greatly exceeds the data. In order to find a reasonable fit between synthetics and data for stations near and far from the Imperial fault, it was necessary to have a highly variable rupture velocity that is extremely fast in certain places on the Imperial fault.

Because the rupture velocity exceeds the shear wave velocity over a fairly large part of the fault, we might expect to see a strong wave front propagating away from the fault at an angle about 35° ($\Theta = \tan^{-1} V_s/V_r$) measured from the strike. After computing synthetic particle velocities due only to the radiation from the Imperial fault segment 10–25 km, the only indication of the fast rupture velocity was the relatively large amplitudes of the 323° component. This indicator is rather weak since our 323° synthetics generally exceed the data for stations farther than 15 km from the fault trace. Nevertheless, if one assumes that the supershear region is between 10 and 25 km on the fault, the maximum effect of the supershear rupture will be most noticeable on the array stations about 12 km off the fault, a distance that corresponds closely with E03 and E11. The 323° component of data changes dramatically between E04 ($y_2 = 6.9$ km) and E03 ($y_2 = 12.6$ km). The waveforms are different, and the peak-to-peak amplitude at E03 is 84% larger than the peak-to-peak amplitude at E04. A similar effect occurs between EDA ($y_2 = -5.3$ km) and E10 ($y_2 = -8.8$ km). The waveforms change, but the peak-to-peak amplitude at EDA is just slightly greater than that at E10. The 323° components at E10 and E11 ($y_2 = -13.0$ km) are similar in amplitude and shape, but at E12 ($y_2 = -18.3$ km) the peak-to-peak amplitude is only about half of the amplitude at E11.

Constraint on Slip Rate Distribution

The gross form of the slip rate distribution (Figure 7) is not that different from *Olson and Apsel* [1982] or *Hartzell and*

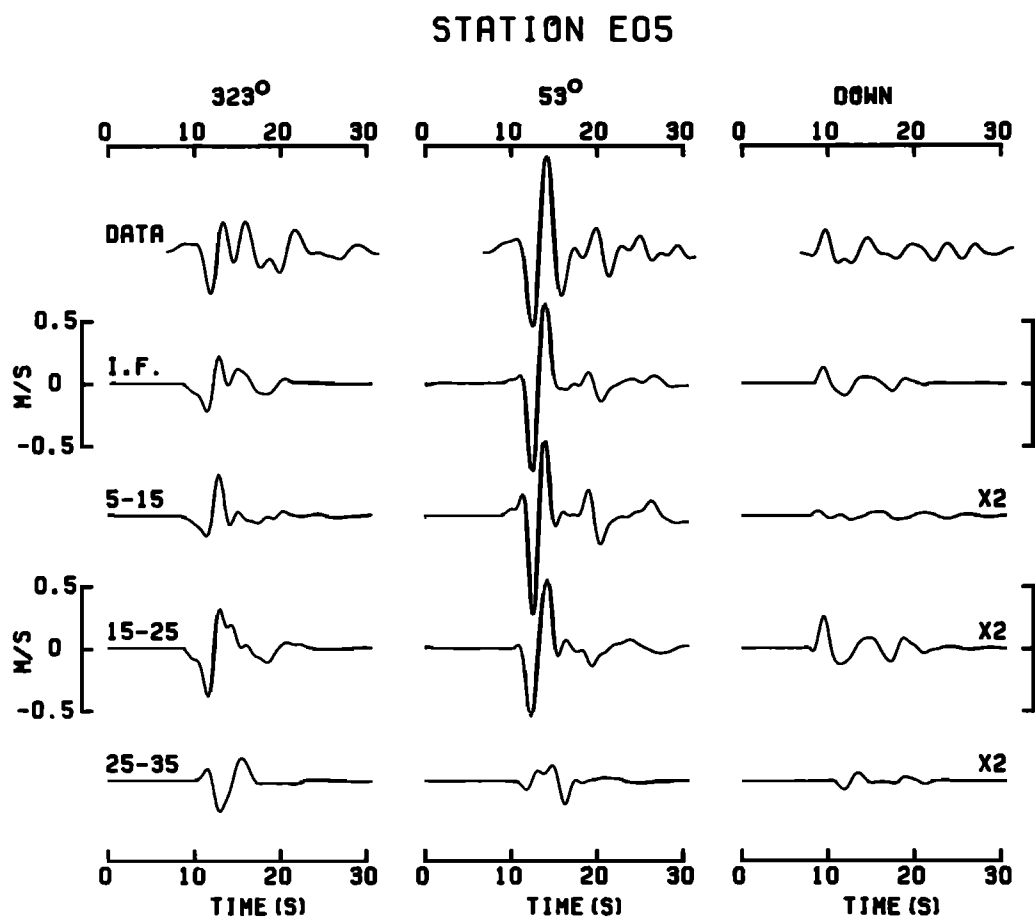


Fig. 14. To illustrate which part of the Imperial fault is the probable cause for the large-amplitude vertical accelerations [see Archuleta, 1982b] and to see the contribution from the fault north of the array stations, the Imperial fault is divided into three segments: 5–15, 15–25, and 25–35 km. The particle velocity, multiplied by 2, from each of these segments is plotted. The leading positive pulse on the vertical component is associated with the large amplitude accelerations. Obviously, the 15- to 25-km range is the primary contributor to this vertical pulse.

Heaton [1983] with the exception of the slip rate in the 25- to 30-km range and our significantly smaller amplitudes at shallow depths. Since the rupture front is moving away from the array stations, it was assumed that slip in this range cannot be well constrained. There are features in the data, however, that do constrain the slip rate north of the array stations, for example, the double positive peaks on the 323° component at E05 and the similarity of the 323° waveforms at E10, E11, and E12, which also show two distinct positive peaks (Figure 3). The second peak is a direct result of faulting north of the array stations. In Figure 14 we show how three 10-km segments (5–15, 15–25, and 25–35) combine to produce the motion at E05. We have deliberately divided the fault such that a division, 25 km, occurs very near the point where the array stations cross the fault. Faulting in the 25- to 35-km segment gives rise to the second peak on the 323° component.

Although the fault was not divided in the same way, the 10-km segments that contribute to the particle motion at E06 and E03 (Figure 13) further demonstrate the need for significant slip rate on the Imperial fault north of the array stations. In fact, without the slip rate contribution north of the array stations, it does not seem possible to match simultaneously the data both near and far from the fault.

A major difference between the distribution of strike-slip

rates found here and those presented by Hartzell and Helmberger [1982], Olson and Apsel [1982], and Hartzell and Heaton [1983] is the size of the amplitudes at depths less than 5 km. In our model we have almost no strike-slip amplitudes greater than 0.2 m/s, whereas the other models indicate slip rates of the order of 0.5–1.0 m/s. In our earlier discussion on the fit between the synthetics and data for stations E05, E06, E07, and E08, we pointed out that small amplitudes in this region were necessary in order that we not produce a large *SS* phase. It was surprising how the Olson and Apsel and Hartzell and Heaton models could tolerate such amplitudes without overdriving the *SS* phase. A hint of how this is allowed in their models is given by comparing the synthetics of Hartzell and Heaton's models W2 and 31, which are quite similar in their distributions of slip in the upper 5 km. Model 31 produces a pronounced *SS* phase almost half as large as *S*, while model W2 produces almost no *SS* amplitude (see Figure 19 of Hartzell and Heaton [1983], stations EL5, EL7, EL8, 230° , and Dif, 0°). Although there are some differences between the model parameters of W2 and 31, the biggest difference is that a given fault element in W2 can radiate at three separate times, whereas in model 31 that particular element can radiate only once. The multiple radiation from a given fault element is also common to the Olson and Apsel faulting model. Since our

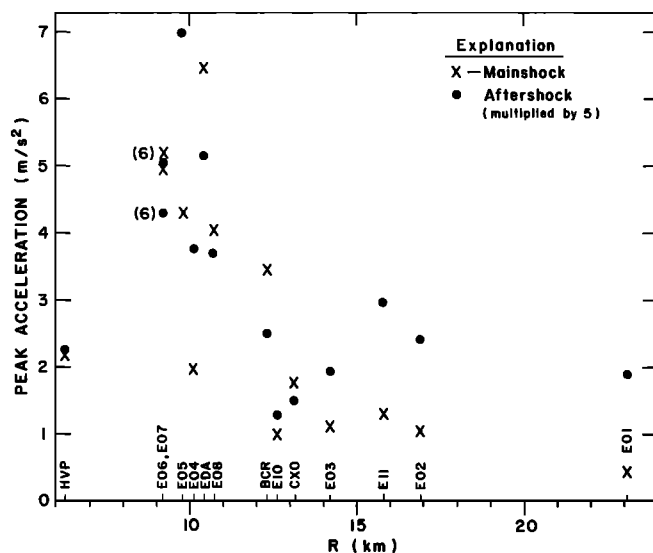


Fig. 15. The peak vertical acceleration (crosses) recorded during the main shock is plotted versus distance from the fault. The peak vertical acceleration due to P waves (solid circles) from an aftershock recorded at the same stations about $2\frac{1}{2}$ min after the main shock have been scaled upward by a factor of 5 and plotted. Note the difference in decay with distance for the main shock and aftershock even though the aftershock hypocenter is very near the assumed source of the large-amplitude vertical accelerations generated during the main shock.

modeling allows a given fault element to slip only once, we have had to reduce the slip rate amplitudes for depths shallower than 5 km to avoid a large SS phase.

Vertical Motion

The last point we want to discuss is a possible explanation of the large-amplitude vertical accelerations (LAVA's) that were observed primarily at stations E05, E06, E07, E08, and EDA. A lengthy description of these vertical accelerations and possible explanations for their origin was given by Archuleta [1982b]. The explanations for these phases fell into two camps: path effect and source effect. Because of the strong P wave velocity gradient in the upper 5 km of the Imperial Valley, slip in the upper 5 km will generate a family of P waves that reflect off the free surface (pP , PP), pass through a caustic, and create large vertical motion in a limited range. To be consistent with the limited range over which the PP phase is a maximum, the slip that generates LAVA's must occur in the sediments about 5–6 km from the hypocenter. To be consistent with the arrival time of these large-amplitude vertical accelerations, the rupture front must reach the area that generates the PP phases in about 2.5 s. The faulting model we have determined (Figure 7) completely contradicts the PP hypothesis. The rupture front does not reach the critical area in the sediments until 4.2 s after the origin time (Table 2). Furthermore, the dominant vertical motion at E05, E06, E07, and E08 comes from the 15- to 25-km range on the Imperial fault (e.g., Figure 14). Because of our rather poor fits to the vertical motion at E06 and E07, it might be argued that nothing definitive can be deduced. At E05 and E08 the synthetic vertical component credibly resembles the data. We have segmented the fault in various ways and are absolutely certain that for our faulting model the 15- to 25-km range is the most important region of

the fault in producing the vertical synthetics (Figure 14). Furthermore, the regions 15–20 km and 20–25 km are equally important in generating the vertical particle velocity. This area is precisely the area where the rupture front has its fastest velocity and its maximum acceleration and deceleration.

The major acceleration and deceleration of the rupture front was the most likely source effect given by Archuleta [1982b] to explain the large-amplitude vertical accelerations, although he pointed out that there was little direct evidence to support such an idea. Olson and Apsel's [1982] results indicate a supershear wave rupture velocity, but it is the change in the rupture velocity and not its actual value that leads to high-frequency radiation [Madariaga, 1977]. The supershear rupture velocity does have the necessary effect of altering the radiation pattern for P waves in that the maxima of the radiation pattern will be pulled in closer to the fault [Madariaga, 1977; Boatwright, 1980]. Of course, our faulting model is based solely on low-frequency particle velocity simulations. However, the leading pulse at low frequency on the vertical components of E05, E06, E07, E08, and EDA is associated with the high-frequency large-amplitude vertical accelerations. Although there is large slip rate in the 15- to 20-km range, the fact that the 20- to 25-km range, where the slip rate is about half what it is in the 15- to 20-km range, contributes almost equally to the vertical motion, suggests that the slip rate amplitude itself, equivalently the local stress drop, is not the principal explanation for the large-amplitude vertical motion.

Further evidence that the LAVA's cannot be attributed only to a large stress drop comes from comparing the vertical accelerations generated by a M_L 5.2 aftershock. Its location, $32^{\circ}46.39'N$, $115^{\circ}25.63'W$, 9.4-km depth, origin time 2319:35 UT (P. Spudich, personal communication, 1983), places it (Figure 6) very near where the large-amplitude vertical accelerations in the main shock must have originated if they are direct P waves [Hartzell and Helmberger, 1982]. Since the radiation from the aftershock was recorded on the same instruments, we can use its radiation as a Green's function [Hartzell, 1978], presuming that its focal mechanism is similar to the main shock at that point. In Figure 15 we have plotted the maximum acceleration anywhere on the vertical component due to the main shock as a function of epicentral distance from the aftershock's epicenter. We have also plotted the maximum vertical acceleration, multiplied by 5, due to the P waves generated by the aftershock. The aftershock accelerations have been multiplied by 5 to agree approximately with the main shock accelerations recorded closest to the Imperial fault. The maximum main shock vertical acceleration at E06 has been divided by 3 [Mueller and Boore, 1981]. The comparison clearly shows that the P wave amplitudes from the aftershock decay with distance much more slowly than the maximum vertical acceleration due to the main shock. At stations E01, E02, E03, and E11 the main shock amplitude is deficient by 1.5, 1.3, 0.8, and 1.6 m/s^2 , respectively (E12 and E13 did not record this aftershock.). Because we selected the maximum vertical acceleration for the main shock, while the maximum P wave acceleration of the aftershock may not have been recorded because the SMA-1 is a triggered instrument, the acceleration discrepancy at each station is a minimum.

Since the data are linearly related to the slip rate amplitude (local stress drop), by equalizing the main shock and after-

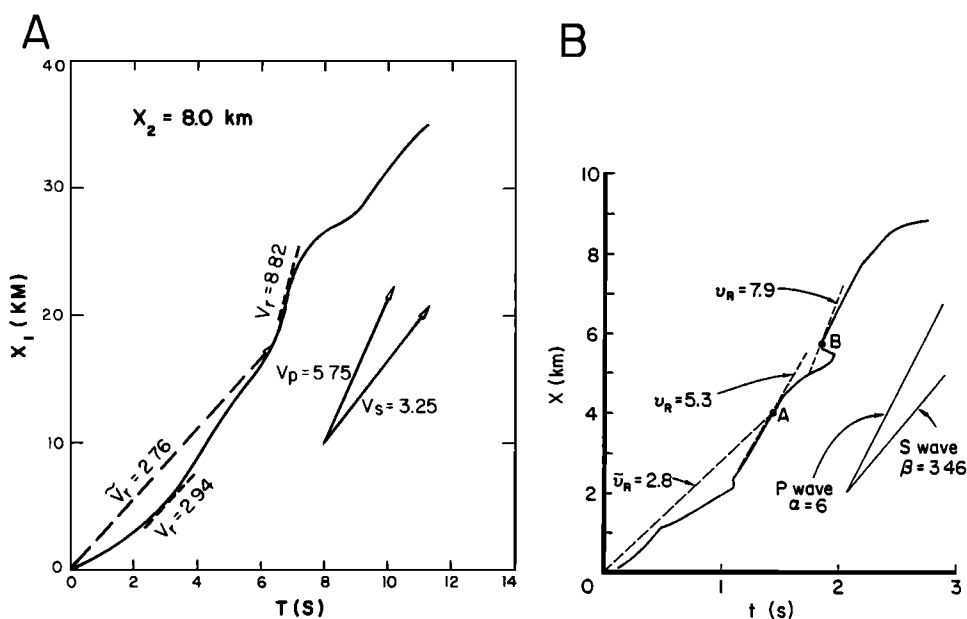


Fig. 16. (a) At the hypocentral depth of 8 km, the rupture time is plotted against distance along strike for our faulting model. The secant (average) rupture velocity \bar{v}_r is simply the position X_1 divided by $T(X_1)$ and is almost everywhere less than the local P wave velocity. However, the tangent (local) rupture velocity is highly variable, sometimes exceeding the local P wave velocity. The rupture starts slowly, accelerates, stays nearly constant to about 17 km, suddenly accelerates, then decelerates, then accelerates to a nearly constant velocity. (b) A similar plot is taken from Day [1982b] for the case of a spontaneous rupture in the presence of nonuniform prestress. Regions where the prestress are close to the yield stress are the regions with locally supershear and supercompressional rupture velocities. (Reprinted with permission of the *Bulletin of the Seismological Society of America*.)

shock accelerations for stations near the fault, we should have nearly equal values far from the fault. This does not happen. Lateral inhomogeneity of the velocity structure is excluded since the origin of the LAVA's is nearly the same as the aftershock hypocenter. We conclude that the dynamics of the main shock, for example, the rupture velocity, strongly influenced the double-couple radiation rather than having a large slip rate or, equivalently, a large stress drop generates the LAVA's.

DISCUSSION

Nonlinearity

In our experience of trying almost 300 faulting models, we found that the synthetic seismograms were more sensitive to variations in the rupture time than any other faulting parameter. As discussed earlier, the rupture time is nonlinearly related to the synthetics. Although we found at least a dozen models that fit some of the data very well, we also found that in order to make any significant improvements to certain groups of data, we would have to make severe changes to the rupture time parameter. Small perturbations to the slip rate parameters or the durations about a given model did not in any way improve certain gross misfits between the synthetics and the data.

The nonlinearity between the data and some of the faulting parameters is one of the primary reasons our model does not resemble the model obtained by either Hartzell and Helmberger [1982] or Hartzell and Heaton [1983]. One of the basic assumptions in both of these analyses is that the rupture velocity is constant or approximately so. Because the inversion results of Hartzell and Heaton supercede the results of Hartzell and Helmberger, we will discuss only the results of Hartzell and Heaton. After parameterizing the faulting parameters they inverted the low passed particle

velocity time histories for a distribution of slip amplitudes in a manner similar to that of Olson and Apsel [1982]. There are major differences between the Hartzell and Heaton method and that of Olson and Apsel [1982], for example, the inclusion of long-period teleseismic P waves and the criterion for stabilizing the numerical method, but the one major difference of interest to us is the parameterization of the rupture time. Olson and Apsel allowed slip to commence in their 5×5 km cells at a time within a 3-s window centered on the time when the rupture front, traveling at 0.9 times the local shear wave speed, arrived at the center of the cell. Hartzell and Heaton used a similar scheme with an important difference, namely, the slip could commence in a 1.7-s window beginning at or after a rupture front traveling at 0.85 times the local S wave velocity arrived at the center of their 2.5×3 km cells. The parameterization by Hartzell and Heaton a priori excludes the rupture time values given in Table 2 for ranges greater than to 15 km. On the basis of our earlier discussion of the rupture time using particle velocities at E03 and E06, we suspect that the parameterization of the rupture time is the primary reason that Hartzell and Heaton's synthetics overestimate the amplitudes for stations near the fault and underestimate the amplitudes off the fault. In the root mean square sense, their inversion is forced to trade off the amplitude misfit for stations near and far from the fault because of the parameterization of the rupture time.

Since the Olson and Apsel model is roughly a gross average of our model, we do not fully understand why their inversion results systematically underestimate the primary horizontal pulses of the low passed accelerograms. A. H. Olson (personal communication, 1982) explained that their method of stabilizing the numerical algorithm eliminates the small singular values. The small singular values are related to the unresolvable parts of the slip distribution. These

unresolvable parts arise from the fact that when the rupture is propagating toward the stations, the radiation is being compressed in time by the rupture. Because of the frequency resolution of their model, the model cannot distinguish how much each part of the fault has radiated.

Regardless of the explanation of the misfit between the synthetics and the data, what is important is that the linear inversion methods of *Olson and Apsel* [1982] and *Hartzell and Heaton* [1983] solve for the slip distribution after an a priori parameterization of the other faulting variables that are not linearly related to the data. Since the slip distributions of these models are approximately similar but the fits between synthetics and data are clearly different, it seems that the parameterization of the nonlinear variables becomes a very critical element. This fact is clearly demonstrated in the work of Hartzell and Heaton, who tried 30 different inversions. Among those 30 inversions are two that are very similar (31 and W2) except for the parameterization of the timing variable. In model 31 the rupture time is determined by a rupture velocity of 0.8 times the local shear wave velocity; in model W2 the rupture time is variable in that slip may commence in any of three time windows after the rupture traveling at $0.85V_s$ reaches an element on the fault. Hartzell and Heaton report, "the best fitting, constant-rupture-velocity inversion, Model 31, does a noticeably poorer job of matching the strong-motion records. The more complicated timing of models W2 and W3 seems to be required by the data."

Because inversion methods are probably more economical than trial and error modeling for analyzing large data sets, we favor using them for future work. While their numerical limitations may be well understood and while their ability to provide quantitative measures of the resolution of the linear variables may be well founded, it is the effect and treatment of the nonlinear variables [*Oldenburg*, 1983] that we must understand. Because of the importance of the rupture time to the synthetics, an inversion method tailored to determining the rupture time should be developed.

Seismic Risk

Of the many inferences one may draw from the faulting model that we have determined, a principal one is that the spectrum of possible earthquake scenarios and related hazards is much broader than normally anticipated. Because high-frequency radiation is directly proportional to changes in rupture velocity [*Madariaga*, 1977], coupled with the possibility that apparent rupture velocities can exceed both the shear and compressional wave velocity for small regions of the fault, high-frequency radiation in the near-source region can be severely modified for both *S* and *P* waves. Amplification of the particle motion for *P* waves is a real possibility. Anomalous amplitudes in certain regions off the fault due to bow wave type propagation become another possibility. Although there is very little theoretical work that delves into the consequences of local rupture velocities exceeding the *S* wave or *P* wave speed, it seems that there is a definite possibility that such a phenomenon can exist as part of an earthquake mechanism. *Bouchon* [1979] used a related phenomenon to explain the particle velocity recorded at station 2 during the 1966 Parkfield earthquake. *S. M. Day* (personal communication, 1982) has computed the particle motion off the fault due to dynamic fractures which have local rupture velocities that exceed the shear wave velocity

and in some cases the compressional wave velocity. Although his results show a more dramatic change in amplitudes recorded off the fault than observed during the Imperial Valley earthquake, they are qualitatively consistent with the faulting model we have proposed. The fact that a faulting model that generates synthetic seismograms consistent with the data has a highly variable and fast rupture velocity certainly suggests that the potential near-source seismic risk can be greater than is commonly assumed.

Earthquake Mechanics

Of course, the faulting model we have presented is purely kinematic. To infer the basic physical processes of the 1979 Imperial Valley earthquake, we rely on the striking similarity between the behavior of our faulting parameters and those determined by *Day* [1982b] for a general dynamic rupture in the presence of nonuniform prestress (Figure 16). *Day* found that in regions where the prestress was close to the yield stress the rupture velocity was faster than the local *S* wave velocity, while in regions where the prestress was far from yield stress, the rupture velocity was slower than the local *S* wave velocity. Furthermore, he found that the maximum slip rate was closely correlated to the rupture velocity, that is, the slip rate would increase (decrease) when the rupture velocity increased (decreased). Except for the region near the hypocenter, a similar correspondence between rupture velocity and slip rate exists in our faulting model (Figure 6), especially in the 15- to 30-km range and depths greater than 5 km. By analogy with *Day's* model, we would infer that the prestress on this area of the fault was near its critical level, especially the small part of the fault in the range 17.5–22.5 km.

At the surface this segment is one of the longest continuous trends of the Imperial fault on which the horizontal offsets were measured [*Sharp et al.*, 1982, Plate 1]. This segment is bounded by two faults. The projection of the Superstition Hills fault intersects the Imperial fault near the southern end of this segment, and the Brawley fault intersects the Imperial fault at the northern end of the segment. At the northern end of this segment the Imperial fault changes strike from 323° to about 315° for about 5 km before resuming its general strike near 323° (Figure 1). (Very near its northern terminus the Imperial fault turns to almost due north.) The interaction of these two faults with the Imperial fault could produce a higher prestress relative to other parts of the Imperial fault. There are two indications that the prestress was higher. First, in the $3\frac{1}{2}$ months preceding the Imperial Valley main shock the background seismicity of the region was generally less than normal [*Johnson and Hutton*, 1982]. However, the one area on the Imperial fault north of the international border which showed seismicity was this 15- to 25-km segment. The second indicator comes from measurements of surface creep on this segment [*Cohn et al.*, 1982]. Both a creep meter and an alignment array show creep on this segment just months before the main shock. Whether the observed creep is due to the aforementioned earthquakes or to a general increase in prestress is not known. Although all the evidence is circumstantial, it does tend to support the idea of a relatively higher prestress on this segment of the Imperial fault.

Although the faulting process is widely recognized as representing inhomogeneous stress release (see *Kanamori* [1981] or *Aki* [1982] for extended references), our faulting

model of the Imperial Valley earthquake used in analogy with the results of Day [1982b] suggests that the weak (prestress close to the yield stress) regions of the fault are the critical regions for influencing the faulting process. In this respect, the Imperial Valley earthquake is a counterexample to the barrier model [Das and Aki, 1977; Aki et al., 1977] in which the strong (prestress far from the yield stress) regions exert the greatest influence on the faulting process. On the other hand, the Imperial Valley earthquake is similar to the asperity model described by Rudnicki and Kanamori [1981] in that regions where slip is occurring are strong regions and asperities are weak regions. There are three stresses to be considered: the yield stress, the prestress, and the sliding frictional stress. Suppose that the frictional stress is a constant everywhere on the fault. For whatever reason, for example, a change in geometry of the fault [Bakun et al., 1980; Reasenber and Ellsworth, 1982] or a change in material properties, certain parts of the fault may increase their prestress level at a different rate from other parts of the fault even though the driving forces or displacements may be uniformly increasing with time. Under the assumptions of the dynamical models [e.g., Andrews, 1976, Das and Aki, 1977, Day, 1982b, Virieux and Madariaga, 1982], the rupture cannot propagate until the prestress equals the yield stress, at which time the stress drops from the yield stress to the sliding frictional stress. Clearly, the hypocenter represents the weakest part of the fault plane since it is the place where the prestress first equals the yield stress. Although the hypocenter is an obvious part of the fault plane that indicates stress inhomogeneity, other parts of the fault may be near failure. It is the fracture of these weaker parts that leads to high rupture velocities and slip velocities [Day, 1982b].

The Brawley fault intersects the Imperial fault very near where the rupture velocity on the Imperial fault suddenly decelerates. As discussed by Rice [1980], additional fractures induced on planes making nonzero angles with the primary fracture plane are an expected means of arresting fracture speeds that are near the critical speeds for inplane and antiplane shear fractures. Because the Brawley fault is about 37° off the strike of the Imperial fault, we would expect to have large shear stresses induced on the Brawley fault, while the normal stress would be reduced. This combination suggests that slip on the Brawley fault was directly triggered by the dynamics of the faulting on the Imperial fault.

SUMMARY

Using a trial-and-error forward kinematic modeling, we computed synthetic particle velocity time histories to compare with the observed low passed near-source velocities of the October 15, 1979, Imperial Valley earthquake. Radiation from rupture on the Imperial fault dominates almost all the near-source ground motion. However, about 8 s after its origin time, rupture on the Imperial fault triggered rupture on the Brawley fault. Radiation from the Brawley fault severely affects certain components of motion at several nearby stations. The geometry and seismic moment of these two faults are given in Table 3. The total combined moment of the Imperial and Brawley faults is 6.7×10^{18} N m, which is very close to the seismic moment of 7×10^{18} N m determined by Kanamori and Regan [1982] from long-period surface waves.

Four faulting parameters (strike-slip rate, dip-slip rate,

TABLE 3. Geometrical and Static Fault Parameters

Parameter	Value	
	<i>Imperial Fault</i>	
Length		35 km
Width		13 km*
Strike		323°
Dip		80° NE
Rake		180°†
Seismic moment		6.4×10^{18} N m
	<i>Brawley Fault</i>	
Length		10 km
Width		8 km
Strike		360°
Dip		90°
Rake		variable
Seismic moment		2.7×10^{17} N m

* For the region near the epicenter, the faulting width is less than 13 km.

† The rake is 180° everywhere except near the northern end, where it becomes variable.

rupture time, and duration) were allowed to vary on the fault planes. The spatial distributions of these parameters for the Imperial fault and the Brawley fault are shown in Figures 6 and 8, respectively. With respect to the Imperial fault these parameters show the following. The maximum strike-slip rates are found for depths greater than 5 km with maximum values of almost 1.0 m/s. Although there is spatial complexity in the distribution of strike-slip rates, the distribution is rather smoothly varying. The dip-slip rate is basically confined to the sediments at the northern end of the Imperial fault. The maximum dip-slip rate is about 0.5 m/s. Because it occurs in the surficial material where the shear modulus is extremely low compared to the deeper material, the radiation from the dip-slip component is not a key element in determining the near-source ground motion. The duration of the slip rate, equivalently the rise time of the dislocation, is also spatially varying with a maximum value of 1.9 s, which is considerably shorter than the total rupture time. Perhaps the most unsuspected feature of the 1979 Imperial Valley earthquake is the complex temporal evolution of the faulting which is described through the rupture time parameter. Basically, the rupture starts slowly, accelerates to a supershear velocity, propagates at this supershear velocity for about 8 km, suddenly accelerates to a supercompressional velocity, suddenly decelerates to a subshear velocity, and again accelerates to a slightly higher velocity (Figure 16a). On average the rupture velocity at depth is about 3.1 km/s, roughly 0.94 times the local shear wave velocity. Of the four faulting parameters we most often varied, the synthetics were most sensitive to changes in the rupture time parameter.

The faulting parameters for the Brawley fault are totally dependent on the faulting parameters for the Imperial fault. Consequently, we cannot claim much resolution of Brawley fault parameters. We did find that it was necessary to have a mixture of strike-slip and dip-slip faulting on a shallow fault. The strike-slip component dominates, but it is active almost entirely at depth. The dip-slip component is smaller and shows a definite increase in amplitude as one moves northward on the fault. The duration monotonically decreases from the south end to the north. The rupture time is set for a rupture propagating at $0.95V_s$. Slip begins about 1.3 s after rupture on the Imperial fault reached the intersection of the

two faults. Thus, for about 4 s, both the Imperial and Brawley faults were simultaneously rupturing. The Brawley fault has a seismic moment of 2.7×10^{17} N m, approximately a magnitude 5.7 earthquake.

This analysis shows that the hypothesis that the large-amplitude vertical accelerations (LAVA's) might be due to a PP phase [Archuleta, 1982b] is totally inconsistent with this faulting model. It remains an open question as to the exact physical process that led to LAVA's. By comparing the distribution of the main shock, peak, vertical accelerations with that of an aftershock we would argue that the rupture velocity is the most critical factor in generating the LAVA's. If the LAVA's were due only to a stress drop released by a nearly constant, subsonically propagating rupture, the LAVA's would have a spatial dependence similar to the vertical accelerations of M_L 5.2 aftershock which occurred on the same part of the Imperial fault as the source of the LAVA's. Differentiating between a stress drop or a change in rupture velocity as the cause of peak accelerations is rather difficult. In the case of the Imperial Valley earthquake it is possible because of the number of near-source accelerographs.

Perhaps the most important result of our kinematic modeling is the increased awareness of the nonlinearity between the rupture time and the data. While the determination of the slip rate amplitudes may be posed as a linear inverse problem [Spudich, 1980], the parameterization of the nonlinear variables, such as rupture time and duration, requires special consideration [Oldenburg, 1983]. On the basis of our experience in trying to find a faulting model for the 1979 Imperial Valley earthquake and the implications of variations in rupture velocity, we would conjecture that determining the spatial variation of the rupture time is the most critical element in specifying any faulting model when the finiteness of the fault cannot be ignored.

Acknowledgments. Foremost I wish to thank Paul Spudich for his elegant programs for computing extended source synthetics without which I could not have attempted the variety of models that led to the results presented in this paper. I also want to thank Paul for our many discussions in the course of this work, including his thoughtful review of a preliminary draft. In a similar vein, I gratefully appreciate the extensive and careful review by Jack Boatwright. I also thank Allen Olson for allowing use of his DWEF program. Steve Hartzell generously provided a copy of his paper with Tom Heaton prior to its publication. Finally, I wish to thank Larry Baker for optimizing some of the computer programs, Bob Sharp for providing a clear geological picture of the Imperial Valley, and the many people through whose efforts the accelerographs were installed and maintained and the accelerograms were processed. Use of trademarks is for descriptive purposes only and does not imply endorsement by the U.S. Geological Survey. This work was supported by the Office of Nuclear Regulatory Research, U.S. Nuclear Regulatory Commission.

REFERENCES

- Aki, K., Seismic displacement near a fault, *J. Geophys. Res.*, **73**, 5359–5376, 1968.
- Aki, K., Strong motion prediction using mathematical modeling techniques, *Bull. Seismol. Soc. Am.*, **72**, (Part B), S29–S41, 1982.
- Aki, K., M. Bouchon, B. Chouet, and S. Das, Quantitative prediction of strong motion for a potential earthquake fault, *Ann. Geophys.*, **30**, 341–368, 1977.
- Anderson, J. G., and P. G. Richards, Comparison of strong ground motion from several dislocation models, *Geophys. J. R. Astron. Soc.*, **42**, 347–373, 1975.
- Andrews, J., Rupture velocity of plane strain shear cracks, *J. Geophys. Res.*, **81**, 5679–5687, 1976.
- Archuleta, R. J., Hypocenter for the 1979 Imperial Valley earthquake, *Geophys. Res. Lett.*, **9**, 625–628, 1982a.
- Archuleta, R. J., Analysis of near-source static and dynamic measurements from the 1979 Imperial Valley earthquake, *Bull. Seismol. Soc. Am.*, **72**, 1927–1956, 1982b.
- Archuleta, R. J., and S. M. Day, Dynamic rupture in a layered medium: the 1966 Parkfield earthquake, *Bull. Seismol. Soc. Am.*, **70**, 671–689, 1980.
- Archuleta, R. J., and S. H. Hartzell, Effects of fault finiteness on near-source ground motion, *Bull. Seismol. Soc. Am.*, **71**, 939–957, 1981.
- Archuleta, R. J., P. Spudich, and A. Olson, Synthetic seismogram studies of an aftershock of the 1979 Imperial Valley, California earthquake, *Seismol. Soc. Am. Earthquake Notes*, **50**, 50, 1979.
- Bakun, W. H., W. H. Stewart, C. G. Bufe, and S. M. Marks, Implication of seismicity for failure of a section of the San Andreas fault, *Bull. Seismol. Soc. Am.*, **70**, 185–201, 1980.
- Boatwright, J., A spectral theory for circular seismic sources; simple estimates of source dimension, dynamic stress drop, and radiated energy, *Bull. Seismol. Soc. Am.*, **70**, 1–27, 1980.
- Boatwright, J., A dynamic model for far-field acceleration, *Bull. Seismol. Soc. Am.*, **72**, 1049–1068, 1982.
- Boore, D. M., and J. B. Fletcher, Preliminary study of selected aftershocks from digital acceleration and velocity recordings: The Imperial Valley, California, earthquake, October 15, 1979, *U.S. Geol. Surv. Prof. Pap.*, **1254**, 109–118, 1982.
- Bouchon, M., Predictability of ground displacement and velocity near an earthquake fault, An example, the Parkfield earthquake of 1966, *J. Geophys. Res.*, **84**, 6149–6156, 1979.
- Bouchon, M., The rupture mechanism of the Coyote Lake earthquake of August 6, 1979, inferred from near-field data, *Bull. Seismol. Soc. Am.*, **72**, 745–758, 1982.
- Brady, A. G., V. Perez, and P. N. Mork, Digitization of processing of mainshock ground-motion data from the U.S. Geological Survey accelerograph network, The Imperial Valley, California, Earthquake, October 15, 1979, *U.S. Geol. Surv. Prof. Pap.*, **1254**, 377–384, 1982.
- Brune, J. N., F. L. Vernon III, R. S. Simons, J. Prince, and E. Mena, Strong-motion data recorded in Mexico during the main shock, The Imperial Valley, California, Earthquake, October 15, 1979, *U.S. Geol. Surv. Prof. Pap.*, **1254**, 319–350, 1982.
- Burridge, R., Admissible speeds for plane-strain self-similar shear cracks with friction but lacking cohesion, *Geophys. J. R. Astron. Soc.*, **35**, 439–455, 1973.
- Burridge, R., and L. Knopoff, Body force equivalents for seismic dislocations, *Bull. Seismol. Soc. Am.*, **54**, 1875–1888, 1964.
- Chavez, D., J. Gonzales, A. Reyes, M. Medina, C. Duarte, J. N. Brune, F. L. Vernon, III, R. Simons, L. K. Hutton, P. T. German, and C. E. Johnson, Mainshock location and magnitude determination using combined U.S. and Mexican data, The Imperial Valley, California, Earthquake, October 15, 1979, *U.S. Geol. Surv. Prof. Pap.*, **1254**, 51–54, 1982.
- Cohn, S. N., C. R. Allen, R. Gilman, and N. R. Gouly, Pre-earthquake and post-earthquake creep on the Imperial fault and the Brawley fault zone, The Imperial Valley, California, Earthquake, October 15, 1979, *U.S. Geol. Surv. Prof. Pap.*, **1254**, 161–168, 1982.
- Das, S., Three-dimensional spontaneous rupture propagation and implications for the earthquake source mechanism, *Geophys. J. R. Astron. Soc.*, **67**, 375–393, 1981.
- Das, S., and K. Aki, A numerical study of two-dimensional spontaneous rupture propagation, *Geophys. J. R. Astron. Soc.*, **50**, 643–668, 1977.
- Day, S. M., Three-dimensional finite difference simulation of fault dynamics: Rectangular faults with fixed rupture velocity, *Bull. Seismol. Soc. Am.*, **72**, 1881–1902, 1982a.
- Day, S. M., Three-dimensional simulation of spontaneous rupture: The effect of nonuniform prestress, *Bull. Seismol. Soc. Am.*, **72**, p. 1881–1902, 1982b.
- Fuis, G. S., W. D. Mooney, J. H. Healy, G. A. McMechan, and W. J. Lutter, Crustal structure of the Imperial Valley region, The Imperial Valley, California, Earthquake, October 15, 1979, *U.S. Geol. Surv. Prof. Pap.*, **1254**, 25–50, 1982.
- Hartzell, S., Earthquake aftershocks of Green's functions, *Geophys. Res. Lett.*, **5**, 1–4, 1978.
- Hartzell, S. H., and T. H. Heaton, Inversion of strong-ground motion and teleseismic waveform data for the fault rupture history

- of the 1979 Imperial Valley, California earthquake, *Bull. Seismol. Soc. Am.*, 73, 1553-1583, 1983.
- Hartzell, S., and D. V. Helmberger, Strong-motion modeling of the Imperial Valley earthquake of 1979, *Bull. Seismol. Soc. Am.*, 72, 571-596, 1982.
- Heaton, T. H., and D. V. Helmberger, Generalized ray models of the San Fernando earthquake, *Bull. Seismol. Soc. Am.*, 69, 1311-1341, 1979.
- Johnson, C. E., and D. M. Hadley, Tectonic implications of the Brawley earthquake swarm, Imperial Valley, California, January 1975, *Bull. Seismol. Soc. Am.*, 66, 1133-1144, 1976.
- Johnson, C. E., and D. P. Hill, Seismicity of the Imperial Valley: The Imperial Valley, California, Earthquake, October 15, 1979, *U.S. Geol. Surv. Prof. Pap.*, 1254, 15-24, 1982.
- Johnson, C. E., and L. K. Hutton, Aftershocks and pre-earthquake seismicity, The Imperial Valley, California, Earthquake, October 15, 1979, *U.S. Geol. Surv. Prof. Pap.*, 1254, 59-76, 1982.
- Johnson, C. E., C. Rojahn, and R. V. Sharp (Eds.), The Imperial Valley, California, earthquake, October 15, 1979, U.S. Geol. Surv. Prof. Pap., 1254, 1-451 pp., 1982.
- Joyner, W. B., and D. M. Boore, Peak horizontal acceleration and velocity from strong motion records including records from the 1979 Imperial Valley, California, earthquake, *Bull. Seismol. Soc. Am.*, 71, 2011-2038, 1981.
- Kanamori, H., The nature of seismicity patterns before large earthquakes, in *Earthquake Prediction, An International Review, Maurice Ewing Ser.*, vol. 4, edited by D. W. Simpson and P. G. Richards, pp. 1-19, AGU, Washington, D. C., 1981.
- Kanamori, H., and J. Regan, Long-period surface waves, The Imperial Valley, California, Earthquake, October 15, 1979, *U.S. Geol. Surv. Prof. Pap.*, 1254, 55-58, 1982.
- Kohler, W. M., and G. S. Fuis, A time-term study of the Imperial Valley, California, *Seismol. Soc. Am. Earthquake Notes*, 54, 67, 1983.
- Kostrov, B. V., Self-similar problems of propagation of shear cracks, *J. Appl. Math. Mech.*, 28, 1077-1078, 1964.
- Madariaga, R., High-frequency radiation from crack (stress drop) models of earthquake faulting, *Geophys. J. R. Astron. Soc.*, 51, 625-651, 1977.
- Maruyama, T., On the force equivalents of dynamic elastic dislocations with reference to the earthquake mechanism, *Bull. Earthquake Res. Inst., Tokyo Univ.*, 41, 467-486, 1963.
- McMechan, G. A., and W. D. Mooney, Asymptotic ray theory and synthetic seismograms for laterally varying structures, theory and application to the Imperial Valley, California, *Bull. Seismol. Soc. Am.*, 70, 2121-2035, 1980.
- Mueller, C. S., and D. M. Boore, Site amplification at El Centro strong motion array No. 6, *Seismol. Soc. Am. Earthquake Notes*, 52, 84, 1981.
- Niazy, M., Source dynamics of the 1979 Imperial Valley earthquake from near-source observations (of ground acceleration and velocity), *Bull. Seismol. Soc. Am.*, 72, 1957-1968, 1982.
- Oldenburg, D. W., Funnel functions in linear and nonlinear appraisal, *J. Geophys. Res.*, 88, 7387-7398, 1983.
- Olson, A. H., and R. J. Apse, Finite faults and inverse theory with applications to the 1979 Imperial Valley earthquake, *Bull. Seismol. Soc. Am.*, 72, 1969-2001, 1982.
- Olson, A. H., J. A. Orcutt, and G. A. Frazier, The discrete wavenumber finite element method of synthetic seismograms, *Geophys. J. R. Astron. Soc.*, in press, 1984.
- Porter, L. D., Data processing procedures for mainshock motions recorded by the California Division of Mines and Geology strong-motion network, The Imperial Valley, California, Earthquake, October 15, 1979, *U.S. Geol. Surv. Prof. Pap.*, 1254, 407-417, 1982.
- Reasenberg, P., and W. L. Ellsworth, Aftershocks of the Coyote Lake, California, earthquake of August 6, 1979: A detailed study, *J. Geophys. Res.*, 87, 10637-10655, 1982.
- Rice, J. R., The mechanics of earthquake rupture, *Proc. Int. Sch. Phys. Enrico Fermi*, 78, 555-649, 1980.
- Rudnicki, J. W., and H. Kanamori, Effects of fault interaction on moment, stress drop and strain energy release, *J. Geophys. Res.*, 86, 1785-1793, 1981.
- Scholz, C. H., Scaling laws for large earthquakes, consequences for physical models, *Bull. Seismol. Soc. Am.*, 72, 1-14, 1982.
- Shannon and Wilson, Inc. and Agbabian Associates, Geotechnical and strong motion earthquake data from U. S. accelerograph stations, 1, *Rep. NUREG-0029*, El Segundo, Calif., 1976.
- Sharp, R. V., Surface faulting in Imperial Valley during the earthquake swarm of January-February 1975, *Bull. Seismol. Soc. Am.*, 66, 1145-1158, 1976.
- Sharp, R. V., J. J. Lienkaemper, M. G. Bonilla, D. B. Burke, B. F. Fox, D. G. Herd, D. M. Miller, D. M. Morton, D. J. Ponti, M. J. Rymer, J. C. Tinsley, J. C. Yount, J. E. Kahle, E. W. Hart, and K. E. Sieh, Surface faulting in the central Imperial Valley, The Imperial Valley, California, Earthquake, October 15, 1979, *U.S. Geol. Surv. Prof. Pap.*, 1254, 119-144, 1982.
- Snay, R. A., M. W. Cline, and E. L. Timmerman, Horizontal deformation in the Imperial Valley, California, between 1934 and 1980, *J. Geophys. Res.*, 87, 3959-3968, 1982.
- Spudich, P. K. P., The deHoop-Knopoff representation theorem as a linear inverse problem, *Geophys. Res. Lett.*, 7, 717-720, 1980.
- Spudich, P., Frequency domain calculation of extended source seismograms, *Eos Trans. AGU*, 62, 960, 1981.
- Switzer, J., D. Johnson, R. Maley, and R. Matthiesen, Western hemisphere strong-motion accelerograph station list—1980, *U.S. Geol. Surv. Open File Rep.*, 81-664, 1-153, 1981.
- Virieux, J., and R. Madariaga, Dynamic faulting studies by a finite difference method, *Bull. Seismol. Soc. Am.*, 72, 345-369, 1982.

R. J. Archuleta, U.S. Geological Survey, 345 Middlefield Road, MS/977, Menlo Park, CA 94025

(Received June 25, 1983;
revised October 31, 1983;
accepted November 1, 1983)